https://dx.doi.org/10.1016/j.ijmecsci.2023.108916

Multi-band Topological Valley Modes of Flexural Waves in Micro-perforated Phononic Plates

Lei Fan[1], Yafeng Chen[1*], Jie Zhu[2†], and Zhongqing Su[1‡]

[1]*Department of Mechanical Engineering, The Hong Kong Polytechnic University, Kowloon, Hong Kong SAR, China*

[2]*Institute of Acoustics, School of Physics Science and Engineering, Tongji University, 200092, Shanghai, China*

ABSTRACT

To develop phononic topological insulators (PTIs) with time reversal invariance, phononic crystals (PCs) are elaborately configurated to ensure the lattice symmetry and meanwhile to open the complete band gap. Particularly, a multi-band PTI requires more complex architecture than its single-band counterpart, leading to extra difficulty in implementation and poor manufacturability of PCs. Here, we present a straightforward and generic design strategy, to realize multi-band PTIs in micro-perforated phononic plates. Rather than using complex surface-mounted or embedded scatterers, the novel phononic plate is micro-perforated with a type of fan-shaped split-ring resonators (SRRs), the multi-modal resonances of which under constrained lattice symmetry induce multiple Dirac degeneracies in flexural-wave dispersions at different frequency scales. The multi-band topological phase transitions are observed, and triple topological band gaps are caused when rotating micro-perforated slots properly. Experimental results agree well with numerical simulation results, both demonstrating triband valley edge-state propagation of flexural waves. In addition, we also prove that the developed

valley PTIs enable the second-order corner modes of flexural waves within the corresponding topological band gaps. Parametric studies further reveal that the emergence of the valley-shaped Dirac degeneracy bands in the developed PTI is insensitive to the plate thickness and slots parameters, and more than three Dirac cones exist in flexural-wave dispersions. The developed micro-perforated plates with SRRs provides a convenient platform for enabling multi-band PTIs with various symmetries, facilitating applications of multi-frequency topological effects of elastic waves in a cost-effective way.

Keywords: *Phononic topological insulators; topological elastic waves; flexural waves; multi-band valley modes; micro-perforated plates; split-ring resonators*

[*] yachen@polyu.edu.hk

[†] jiezhu@tongji.edu.cn

[‡] zhongqing.su@polyu.edu.hk

1. Introduction

Recent advances in topological insulators (TIs) [1] have provided new routes for manipulating mechanical waves in rather unique manners [2-5]. Of particular interests are specific edge and corner modes of TIs, protected by nontrivial topology [1], for steering waves, in virtue of their immunity to structural perturbations such as geometric defects and disorders. Somewhat diverse phenomena created by specific TIs have been extensively exploited in wave physics and engineering, to accommodate needs such as one-way wave transmission [6], energy trapping [7-8], and beam splitting [9]. As far as elastic (or mechanical) waves concerned, phononic crystals (PCs), a type of man-made periodic solid materials, have offered a convenient platform to realize mechanical TIs [10]. In particular, the phononic topological insulators (PTIs) [11-14] have been a subject of intensive research in the past decade, rendering numerous application opportunities for mechanical wave manipulations in a broad range from low-frequency vibrations to ultrahigh-frequency phonons [15].

Early strategy for developing PTIs lies on breaking the time reversal symmetry (TRS) so as to imitate the quantum Hall effect [16-17]. Such a strategy requires active elements or external energy inputs that can be factors to narrow the application spectrum of PTIs. In view of this, attempts have been made to explore the possibility of creating PTIs in a fully passive fashion. In this connection, the pseudo-spin [4] and valley PTIs [5], which work independently of any active element or external energy input, are remarkable breakthroughs. Particularly, these PTIs rely solely on the lattice symmetries [18] such

as widely utilized C_3 [19-20], C_4 [21] and C_{6v} [22-23] symmetries to enable topological band gaps, which are straightforward to be constructed in PCs. However, one of the key limitations of most of the pseudo-spin and valley PTIs is the single-band frequency for topologically nontrivial edge and corner mode, restricting them in multiband applications.

More recently, great effort has been made to achieve dual-band or multi-band PTIs, which require a higher degree of structural complexity than its single-band counterpart. In acoustic domain, it has been demonstrated that arranging well-shaped C_3-symmetry scatterers with a hexagonal lattice can induce more than one Dirac degeneracies at the K and K' points of the Brillouin zone, resulting in dual-band or multi-band valley Hall acoustic topological insulators [24-26]. Jia *et al*. [25] experimentally demonstrated the valley sonic crystals with topological refraction at two separated band gaps. Huang *et al*. [26] proposed a lattice superposition mechanism for building multi-band acoustic topological insulator. Nevertheless, different from acoustic waves, the elastic waves in plate structures, with sophisticated Lamb wave modes, see more difficulty in opening multiple complete topological band gaps. This difference can also be reflected in their wave motion equations: extensively studied flexural waves in thin plates are described by a fourth-order differential equation [27], in contrast to acoustic waves which are defined by the second-order differential equations [28]. As a result, prevailing PTIs rely on surface-mounted or embedded scatterers in plates [29-41] to induce topological complete band gaps, at the cost of increasing the complication in manufacturing. It is yet a challenging issue to open multi-frequency topological band gaps in a phononic plate made by a single material without employing those attached scatterers.

Noting that two prerequisites need to be satisfied for achieving multi-band PTIs that preserve the time reversal symmetry (TRS): the lattice symmetry and the multiple complete band gaps. To this end, prevailing forward designs are time-consuming especially when the number of desired topological gaps exceeds two. Moreover, existing dual-band or multi-band valley PTIs commonly suffer from geometrically complex realizations [42-45]. For illustration, Xu et.al [43] achieved dual-band elastic valley effects in hexagonal-lattice phononic crystal plates with a pair of triangular prisms. Liu et.al [44] realized multi-band valley Hall effects in an elastic system composed of beam and rods. Apparently, these structures require the assembly of complex mechanical scatterers, and most designs are proved of effectiveness only in numerical simulation without adequate experimental validation. In addition to forward designs, another available method for creating dual-band and multi-band PTIs is the inverse design [46-47], such as topology optimization [48-51]. However, the existing inverse-optimization works focus more on elastic waves in two-dimensional (2D) planar media such as the out-of-plane mode of PCs [46-51], and relevant exploration on elastic plate structures is rare.

Hitherto, impending needs are calling for multi-band PTIs for robustly steering flexural waves in plate structures using generic and simple architectures. In recognition of this, we here propose a new perforation fashion in plain (without stubbed surfaces) plate structures, to realize multi-band topological valley modes of flexural waves. This design strategy only relies on easily achievable micro-perforations in plate-type structures, completely removing the need for surface-mounted or embedded scatterers employed

in existing PTIs [29-41]. Notice that leveraging penetrations in plain plates is one existing paradigm for designing PTIs [52-58]. Yu *et al*. [53] demonstrated an elastic quantum spin Hall effect in a plain plate consisting of identical perforated holes in wavelength scales. Jiao *et al*. [56] observed topological valley waveguide transport of elastic waves in a thin plate perforated with snowflake holes. However, these PC structures heavily rely on the strict fine-tuning of the sizes of perforated holes and distances among them to enable one satisfactory degeneracy capable of opening a complete band gap. On the other hand, the majority of them only give rise to a single-frequency degeneracy that induces one topological band gap. Different from existing perforation fashions, our approach is to carve out a type of fan-shaped split-ring resonators (SRRs) [59] in a plain plate, the rich multi-modal resonances of which contribute to multiple Dirac degeneracies. Moreover, the resulting Dirac degeneracy bands always maintain valley-shaped irrespective of the plate thickness and slots parameters, with the ease of opening complete topological band gaps. Although the proposed multi-band PTI is demonstrated on a 1 mm thick micro-perforated plate at vibration and ultrasonic frequencies in this paper, underlying mechanics and physics are scale-independent and almost applicable to all plate-type structures (both thin and thick plates) at various frequency scales.

The rest of the article is organized as follows: In Section. 2, band structures of the designed PTI are computed, and triband topological phase transitions are verified accordingly. In Section. 3, triband valley edge modes, along with the edge-state propagation of flexural waves are validated by simulations and experiments. In Section. 4, these topological band gaps are experimentally demonstrated to accommodate

second-order corner modes that are highly localized at corner sites. In Section. 5, parametric study is performed to investigate the effects of geometric parameters on those Dirac degeneracy bands, and to reveal the existence of more than three Dirac cones. Finally, Section. 6 concludes a brief summary.

2. Band structures and topological phase transitions

In this section, the band structures of the proposed PCs are calculated and their topological properties including topological phase transitions and topological invariants are analyzed and discussed.

2.1 Band structures

To create a phononic plate, the homogenous aluminum (Young's modulus $E = 70\times10^9$ Pa, density $\rho = 2700$ kg/m^3, and Poisson's ratio $v = 0.33$) plate (thickness h =1 mm) is perforated with a series of micro-slots periodically arranged with a hexagonal lattice, as depicted in Fig. 1(b). Figure 1(a) presents the unit cell of proposed phononic plate (lattice constant $a = 25$ mm), where thin slots with C_3 rotational symmetry is located at the center of unit cell. The main geometric parameters of slots involve: the outer radius $r = 11.5$ mm, the rib width $e = 3$ mm, the slot width $t = 1$ mm, and orientation angle θ (the angle between central axis of the upper right rib and positive x-axis), as seen in the left panel of Fig. 1(a).

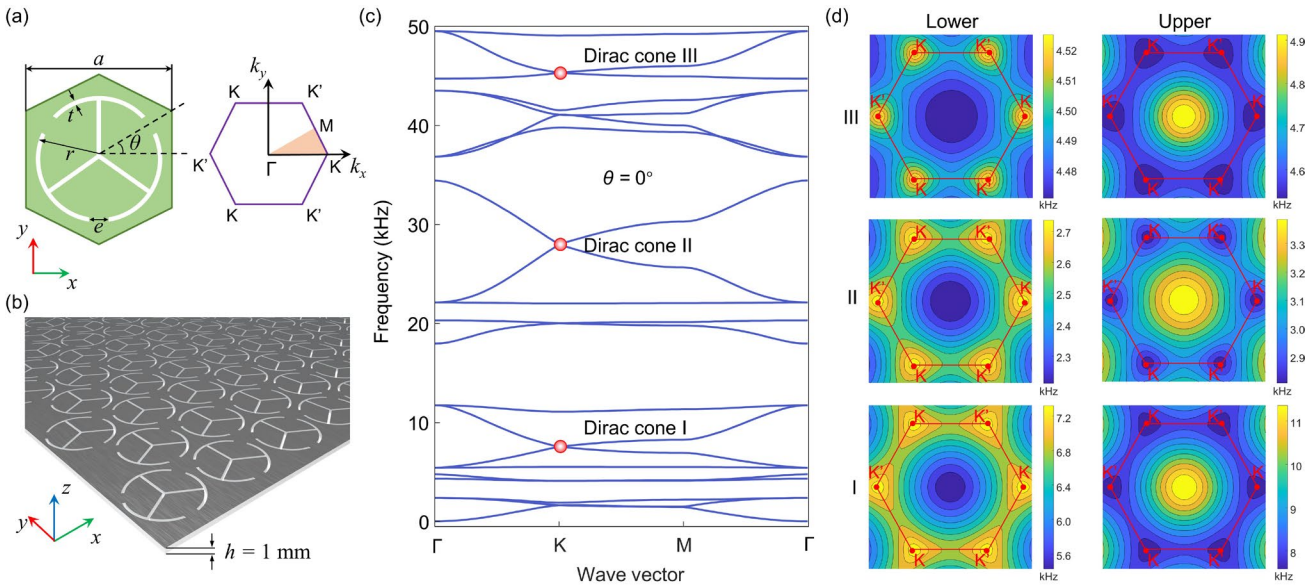

Fig. 1. (a) Top view of unit cell and its irreducible Brillion zone, and main parameters of slots include the outer radius r, the slot width t, and the rib width e. Defined orientation angle θ refers to the angle between the central axis of the upper right rib and positive x-axis. (b) Three-dimensional (3D) schematic diagram of micro-perforated phononic plate. (c) Numerically calculated band structure when $\theta = 0°$, in which blue curves represent flexural waves and three Dirac cones are labeled with red dots. (d) Contour plot of the upper and lower bands for each Dirac cone, where colors represent frequencies.

Next, the band structure (dispersion) of the phononic plate is computed based on numerical finite element (FE) method. Given the flat-surface property of concerned phononic plates, the Mindlin plate theory [60-61] is employed to obtain dispersions instead of three-dimensional (3D) solid full-wave simulation. Since we focus on flexural waves in this work, the wave motion equations of out-of-plane displacement u_z in plates can be formulated as [60-61]:

130
$$\begin{cases} \dfrac{\partial}{\partial x}\left[\kappa\mu h\left(\dfrac{\partial u_z}{\partial x}-\psi_x\right)\right]+\dfrac{\partial}{\partial y}\left[\kappa\mu h\left(\dfrac{\partial u_z}{\partial y}-\psi_y\right)\right]=\rho h\dfrac{\partial^2 u_z}{\partial t^2}, \\ \dfrac{\partial}{\partial x}\left[-D\left(\dfrac{\partial \psi_z}{\partial x}+v\dfrac{\partial \psi_z}{\partial y}\right)\right]+\dfrac{\partial}{\partial y}\left[-\dfrac{D(1-v)}{2}\left(\dfrac{\partial \psi_x}{\partial y}+\dfrac{\partial \psi_y}{\partial x}\right)\right]-\kappa\mu h\left(\dfrac{\partial u_z}{\partial x}-\psi_x\right)=-\dfrac{\rho h^3}{12}\dfrac{\partial^2 \psi_x}{\partial^2 t}, \\ \dfrac{\partial}{\partial x}\left[-\dfrac{D(1-v)}{2}\left(\dfrac{\partial \psi_x}{\partial y}+v\dfrac{\partial \psi_y}{\partial x}\right)\right]+\dfrac{\partial}{\partial y}\left[-D\left(v\dfrac{\partial \psi_x}{\partial x}+\dfrac{\partial \psi_y}{\partial y}\right)\right]-\kappa\mu h\left(\dfrac{\partial u_z}{\partial y}-\psi_y\right)=-\dfrac{\rho h^3}{12}\dfrac{\partial^2 \psi_y}{\partial^2 t}. \end{cases} \quad (1)$$

131 where κ is the shear correction factor accounting for the z-direction variation of
132 transverse shear stress, $D=\frac{Eh^3}{12(1-v^2)}$ is the flexural stiffness of the plate, and
133 $\mu=\frac{E}{2(1+v)}$ is the shear modulus of the aluminum.

134 Then, the above wave motion equations Eq. 1 can be deduced as a general eigenvalue
135 problem by FE discretization [62]

$$\left(\mathbf{K}(\mathbf{q})-\omega(\mathbf{q})^2\mathbf{M}\right)\mathbf{u}=\mathbf{0} \quad (2)$$

136 This eigenvalue problem is solved by combining with the Bloch theory [62]

$$\mathbf{u}(\mathbf{r},\mathbf{q})=\mathbf{u}_{\mathrm{q}}(\mathbf{r})e^{i(qr+\omega t)} \quad (3)$$

137 where Bloch wave vectors q = (k_x, k_y) are swept along the boundary of the first
138 irreducible Brillion zone (IBZ), as boxed by orange color in the right panel of Fig. 1(a).
139 The accuracy of Mindlin plate theory can be guaranteed as it considers shear
140 deformations and rotational effects [60-61]. The comparison with the result calculated
141 by 3D solid full-wave FE simulations can be found in Appendix A. Moreover, using the
142 plate theory is very effective to exclude those unwanted in-plane vibration modes in
143 resulting dispersions. Thus, dispersion curves in all band structures (if not specifically
144 stated), throughout this paper, only represent flexural wave modes while other in-plane
145 modes are unshown.

Figure 1(c) depicts the flexural-wave band structure below 50 kHz when $\theta = 0°$. Three degeneracy points are discovered at K points of the Brillion zone, corresponding to so-called Dirac cones (proved in the following), as labeled by red dots. These three Dirac cones I-III occur at frequencies 7.545 kHz, 27.978 kHz, and 45.322 kHz, respectively, accordingly formed between the 7^{th} and 8^{th}, the 13^{th} and 14^{th}, the 19^{th} and 20^{th} dispersion branches. It is worth noting that degeneracies also exist at K points of other dispersion branches, but they have been examined not to be effective Dirac cones capable of opening complete topological band gaps. In Fig. 1(d), from contour plots of the upper and lower band of each Dirac cone, one can clearly identify that degeneracies of each pair of dispersion bands exactly occur at K and K' valleys of the IBZ, as indicated by the lowest valleys of bands (red dots in Fig. 1(d)). On the formation of these multi-frequency Dirac cones at K (K') points, it is relevant to the multi-modal resonances of perforated three fan-shaped SRRs under constrained symmetry. Bloch eigenmodes at these Dirac cones and relevant discussion can be found in Appendix B.

2.2 Multi-band topological phase transitions

Noted that the Dirac degeneracies at K and K' valleys originate from the C_{3v} symmetry when $\theta = 0°$, and can be lifted up when rotating the orientation angle θ to break the inverse symmetry [34,37,39,40]. For clarity, we choose a unit cell with $\theta = -30°$, named as PC-A, and examine its dispersion. The band structure of the PC-A in Fig. 2(a) shows that, when $\theta = -30°$, three Dirac cones have been lifted up, leading to three complete band gaps, named as BG I, BG II, and BG III correspondingly. The associated frequency ranges of these three band gaps are 6.875-8.056 kHz, 26.010-28.262 kHz, and 46.646-48.617 kHz, respectively. The red and blue colored curves in Fig. 2(a) distinguish vortex

chirality of energy flows at K valleys, which will be elucidated in the following.

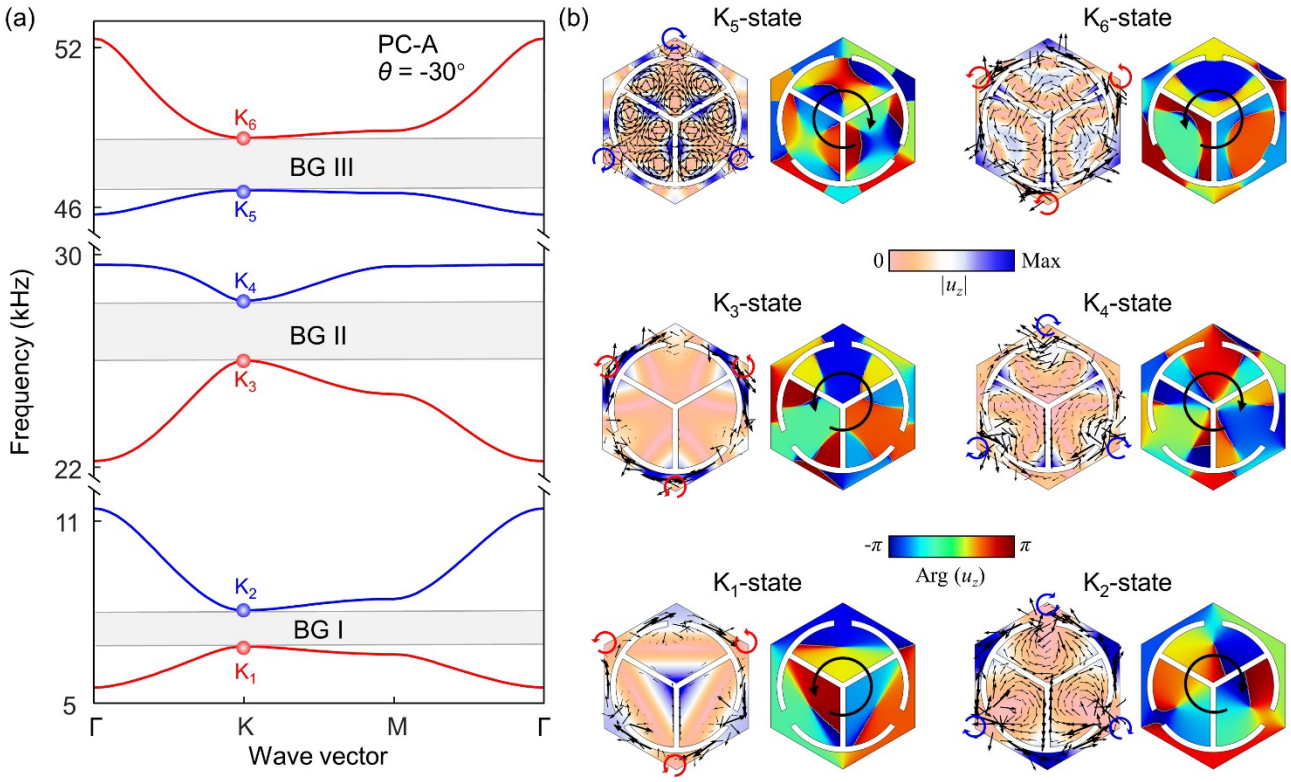

Fig. 2. (a) Upper and lower bands for each Dirac cone when $\theta = -30°$, where three Dirac cones have been opened to form three band gaps: BGs I-III (gray shaded regions). In (a), red and blue colours denote anti-clockwise and clockwise pseudospin orientations at K valleys, respectively. (b) In-plane energy flows (left panel) and phase fields of u_z (right panel) for K_1-K_6 points labelled in (a). The red and blue colored arrows at vertices of unit cells show vortex chirality of energy flows, and black colored arrows in phase fields represent the orientation of phase increasing (orbital angular moment).

Next, we examine valley physics and topological properties of BGs I-III. In condensed matter physics, the quantum valley Hall effects (QVHEs) [64-67] are realized by introducing angular rotation of the electronic wave function at points K and K' in the IBZ [34], which provides an intrinsic magnetic moment in analogy with the one provided by the electronic spin. Similarly, the vortex chirality of elastic energy flow can

be called pseudospin [68,69], which provides a new degree of freedom for elastic waves. In Fig. 2(a), the six K valleys of upper and lower bands of BGs I-III are labeled as K_1-K_6 for the PC-A, where K_1, K_3, K_5 mean K valleys of lower bands, and K_2, K_4, K_6 represent K valleys of upper bands. Fig. 2(b) presents out-of-plane displacement fields $|u_z|$ along with in-plane energy flux (pseudo-spin), and the phase distributions of u_z for the PC-A at K_1−K_6. It is clearly seen that energy flow of K_1-state rotates around three vertices of the unit cell with anti-clockwise direction, as labeled by red colored arrows. Meanwhile, the phase distribution of u_z also exhibits clockwise increase around the center of the unit cell, forming an OAM. On the contrary, the energy flux of K_2-state is observed to revolve around another three vertices of the unit cell, but in an anti-clockwise direction (blue colored arrows). Also, the phase distribution of K_2-state increases anticlockwise. Therefore, the valley features (pseudospin orientations and OAMs) of K_1-state and K_2-state are certainly opposite with each other. For another two

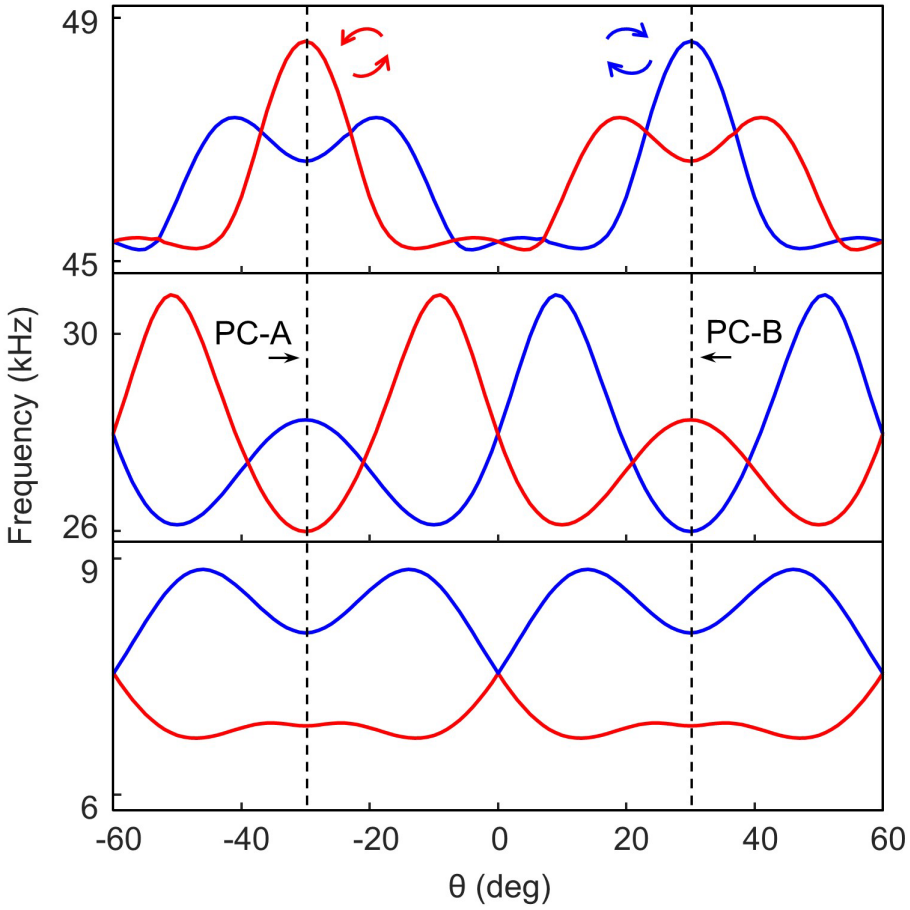

Fig. 3. Evolutions of frequencies of upper and lower bands at K points for Dirac cones I-III (from bottom to top) as a function of the orientation angle θ changing from −60° to 60°. The PC-A and PC-B refer to the unit cells with $\theta = -30°$ and $\theta = 30°$ (black dashed lines), respectively. Red (anti-clockwise) and blue (clockwise) colors represent pseudospin orientations at K valleys.

pairs of K valleys, (K_3, K_4) and (K_5, K_6), energy flux and phase distributions are also indicated to be opposite with each other, as depicted in Fig. 2(b). Note that the phase distributions of u_z exhibit accelerated changes at higher frequencies due to the shorted wavelength.

The above analysis shows that lower and upper bands of BGs I - III possess different valley natures, which can be reversed with the process of topological phase transitions

[2-5]. For better illustration, the evolution of eigenfrequencies (at K points) of upper and lower bands for each Dirac cone, is recorded as θ changes from −60° to 60°. Figure 3 clearly shows that there exist transition points of closing and reopening each Dirac cone of dispersion bands with continuously altered orientation angle θ. Moreover, pseudospin orientations at valleys K of each band are tracked, distinguished by red (anti-clockwise) and blue (clockwise) colors. It can be seen that pseudospin orientations of upper and lower bands for each Dirac cone are indeed reversed as dispersion bands closes and reopens every time. This indicates that topological phase transitions occur at three different frequency ranges by rotating θ, leading to multi-band topologically nontrivial valley PCs. Notably, there exist multiple phase transitions for Dirac cones II and III with θ changing from −60° to 60°. Rigorously, in the following, we calculate the topological invariants of one PC of three band gaps to further confirm that it is indeed topologically nontrivial. The candidate PC is still PC-A with $\theta = -30°$, given that it has a relatively broad bandwidth for BGs I-III. In addition, another PC that has opposed valley topological phases with PC-A needs to be chosen, to hold edge modes between them. Here, we choose PC-B with $\theta = 30°$ since it has the identical band structure but opposite valley pseudospin with PC-A, as pointed out by black dashed lines in Fig. 3.

2.3 Berry curvatures and valley Chern numbers

Next, we evaluate topological invariants of PC-A within BGs I-III. Berry curvature is a gauge-independent local description of the topological invariants in reciprocal space [70,71]. Integrating the Berry curvature over the Brillouin zone gives rise to Chern number, which characterizes the topological nature of Hall insulators [65,70,71]. However, the Berry curvature of valley Hall topological insulators always exhibits local extremes at K and K' valleys but its integration over the Brillouin zone is zero. Therefore,

topological invariant of valley Hall insulator is characterized by a pair of valley Chern numbers [29-30,36-37], corresponding to the local integration of Berry curvature near K or K' valleys. We then evaluate the Berry curvatures B_n of upper and lower bands for BGs I-III of PC-A, which is defined as

$$B_n(\mathbf{k}) = \nabla\mathbf{k} \times \left\langle U_n(\mathbf{k}) \middle| i\nabla\mathbf{k} \middle| U_n(\mathbf{k}) \right\rangle \tag{4}$$

where $U_n(\mathbf{k})$ denotes the eigenmode of the n^{th} band calculated at the wave vector $\mathbf{k}$ and ∇ is the gradient operator.

The integration of the Berry curvature is performed near K valley (K_1-K_6), which gives rise to valley Chern numbers C_v. The valley Chern number C_{v-n} of the n^{th} band yields

$$C_{v-n} = \frac{1}{2\pi}\int_v B_n(\mathbf{k})\, d^2\mathbf{k} \tag{5}$$

The above computation is numerically carried out by the Livelink of COMSOL with MALTAB. The integration domains Δk_x and Δk_y are centered around each K valley in the reciprocal space: from $-0.5\ \pi/a$ to $0.5\ \pi/a$ for Δk_x and from $-0.5\ \pi/a$ to $0.5\ \pi/a$ for Δk_y, which are discretized into 40×40 subdomains to guarantee the convergence.

Figure 4 shows the Berry curvature distributions near K valleys (K_1-K_6) of the upper and lower bands of BGs I-III, respectively. Berry curvature is highly concentrated around respective K valleys of the Brillouin zone, but always with a pair of opposite values for each pair of valleys. For example, Berry curvature around K_1 is negative with an integrated valley Chern number C_v being -0.2757 while Berry curvature around K_2 along with integrated valley Chern number are exactly opposite to those of K_1. Similar phenomena can be observed for another two pairs of valleys, and their integrated

valley Chern numbers are ∓0.2739 for (K_3, K_4) and ±0.1615 for (K_5, K_6), respectively. Noted that our calculated valley Chern numbers are less than the theoretical values ±1/2 [37], mainly due to the wide band gaps and strong space-inversion symmetry breaking [72-73]. Indeed, these types of calculations have been considered of lacking enough precision because they heavily rely on the discretization of the wave vector and normally ignore the overlapped Berry curvatures between the nearby valleys [72,73]. Despite this, the opposite Berry curvatures and valley Chern numbers for each pair of valleys enable us to distinguish the valley topological phases from two different PCs, still with the ability of causing edge modes protected by their nontrivial band topology.

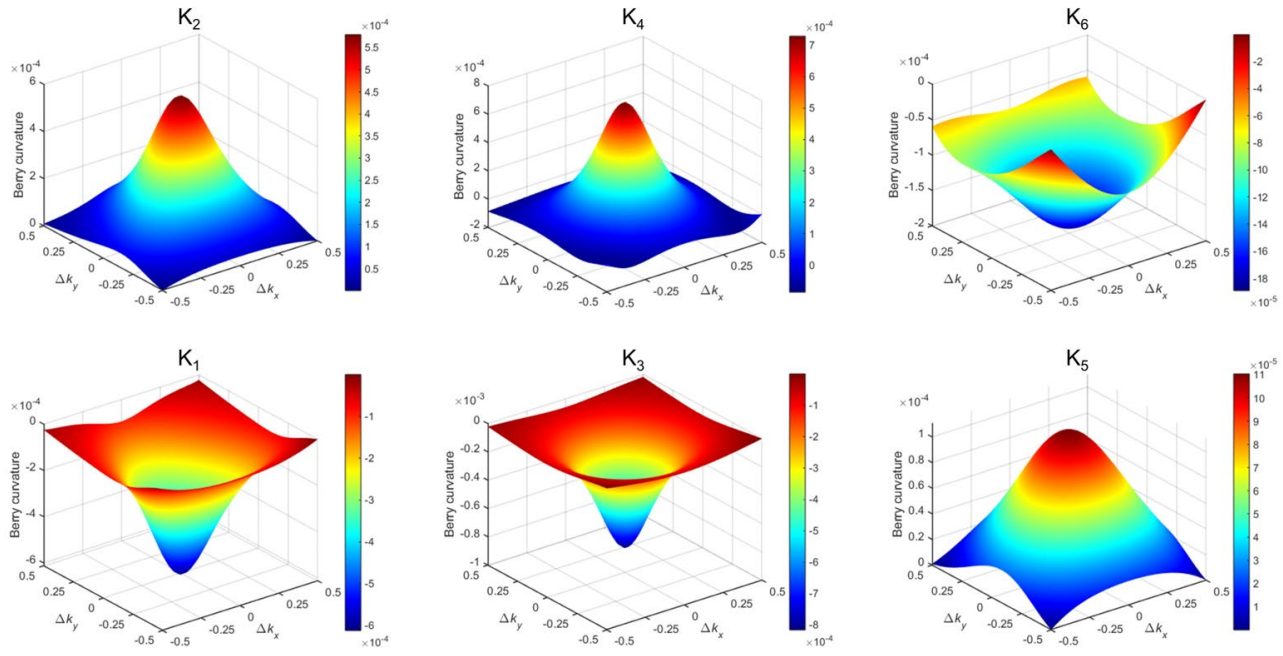

Fig. 4. Berry curvatures near K_1 - K_6 for PC-A. For each K valley, the calculation range (Δk_x and Δk_y) is from −0.5 π/a to 0.5 π/a centred at K points.

Regard to PC-B with $\theta = 30°$, its band structure is completely identical with the one of PC-A while its Berry curvature along with valley Chern numbers at K and K' valleys

have been examined to be just opposite with those of the latter, within all BGs I-III. Combining their opposite pseudospin orientations presented in Fig. 3, these facts allow us to conclude that PC-A and PC-B have distinct valley topological phases within all three band gaps, implying that multi-band edge modes arise at the domain wall connecting PC-A and PC-B.

3. Edge modes and wave propagation along topological interfaces

In previous section, we have revealed that PC-A and PC-B have distinct valley topological phases within BGs I-III. According to the bulk-edge correspondence of valley PTIs [29-30,36-37], topological edge modes are expected to appear at the interfaces (domain walls) between them. To confirm the edge modes, we simulate the supercell dispersions and then experimentally demonstrate edge-state propagation of flexural waves along topological interfaces in finite-sized phononic plates over three concerned frequency ranges.

3.1 Supercell dispersion

Topological edge modes can be directly visualized by the supercell dispersion [2-5]. The black dashed line of Fig. 5(a) boxes the calculated ribbon-shaped supercell comprised of three layers of PCs: PC-A in the upper and lower domains, between which PC-B is sandwiched. Consequently, the supercell contains two types of interfaces, depending on the order: Ψ_{AB} between PC-A (top) and PC-B (down), and Ψ_{BA} between PC-B (top) and PC-A (down), as pointed out by blue and red colored dashed lines in Fig. 5(a). In simulations, Floquet-Bloch periodic boundary condition is applied to the lateral surfaces

along x-axis while upper and lower boundaries are set to be free.

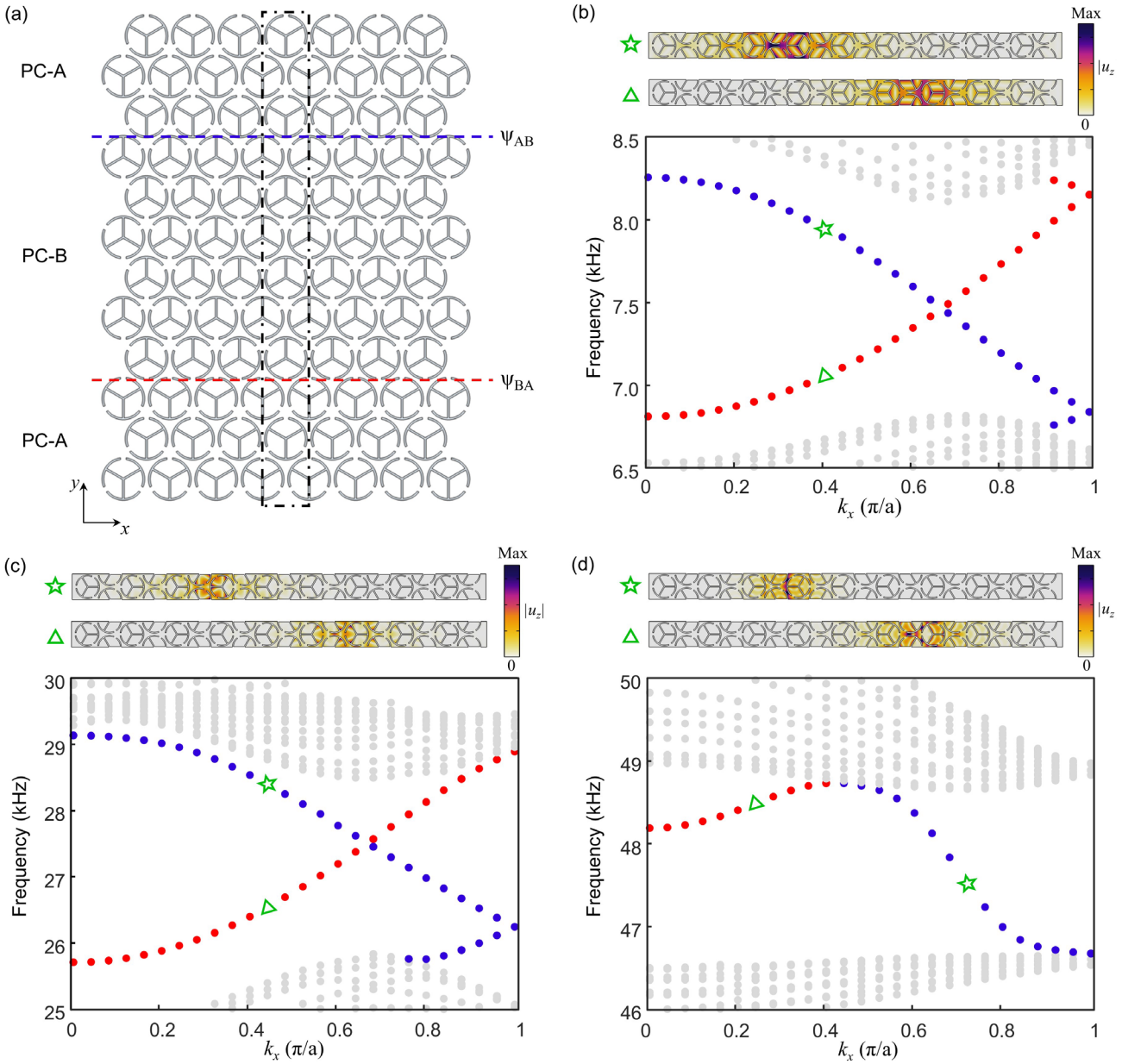

Fig. 5. (a) Calculated ribbon-shaped supercell, which is boxed by black dashed lines. Blue and red colored dashed lines represent the interfaces Ψ_{AB} and Ψ_{BA}, respectively. The projected supercell dispersions and displacement fields $|u_z|$ of selected eigenmodes (green triangles and stars) around frequencies of (b) BG I, (c) BG II, and (d) BG III. The gray dots represent bulk modes while blue and red dots represent edge modes at interfaces Ψ_{AB} and Ψ_{BA}, respectively.

Figures 5(b)−(c) present the dispersion curves around concerned frequencies of BGs I-III, where blue and red colored dots stand for the edge modes at the interface Ψ_{AB} and the interface Ψ_{BA} respectively while gray dots represent the bulk modes. We show displacement fields of $|u_z|$ of those selected edge-state eigenmodes (green stars and triangles in Figs. 5(b)-(c)) within BGs I-III, and identify that these modes are highly localized at the interfaces connecting two nearby domains, which exactly identifies topological edge modes.

One noteworthy phenomenon is that the edge mode at the interface Ψ_{BA} within BG III is not across the entire bulk gap, that is, a frequency gap exists between the edge mode and lower bulk modes, seeing red dots in Fig. 5(d). This can be attributed to a fact that valley Hall topological insulator is also a second-order topological insulator [54,76], which enables a gapped edge mode accommodating corner modes. Since corner modes based on the valley degree of freedom has been proved to be interface-dependent [54,76], edge modes at interfaces Ψ_{BA} and Ψ_{AB} are different: one is gapped while another is gapless, as reflected by red and blue colored edge modes in the supercell dispersion of Fig. 5(d). The demonstration of the corner mode appearing within this edge gap at the interface Ψ_{BA} within BG III is presented in Section. 4.1.

3.2 Experimental demonstration of valley edge-state propagation

To verify the above simulation results, experiment specimens are prepared with two 6061-aluminum alloy plates (the size of 360 × 360 mm^2) fabricated by laser cutting technology: one contains the interface Ψ_{AB} while another contains Ψ_{BA}, the geometric parameters of which are identical with those in previous numerical models. The experiment setups involve the Polytec scanning laser vibrometer (PSV-500), the power

amplifier (Aigtek), and lead zirconate titanate piezoelectric ceramic (one PZT with 6 mm diameter and 1 mm thickness, placed at one side of the plate), as displayed in Fig. 6(a). Figure 6(a) illustrates the entire signal flow for experimentally measuring vibration responses: one PZT disk connected with the power amplifier receiving signals from the controller, is placed at the entrance of the interface to mimic a point excitation source; the laser-captured out-of-plane velocity signals at targeted positions are then sent back to the controller for acquiring the responses. All laser-scanned positions (blue dots) are labeled on the specimens in Fig. 6(c). The excitation signals adopt the periodic up-chirp mode, the swept frequency range of which is 2-50 kHz covering BGs I-III. Measured time-domain signals are post-processed by the controller via fast Fourier transformation (FFT) and then response spectra of scanned points are obtained.

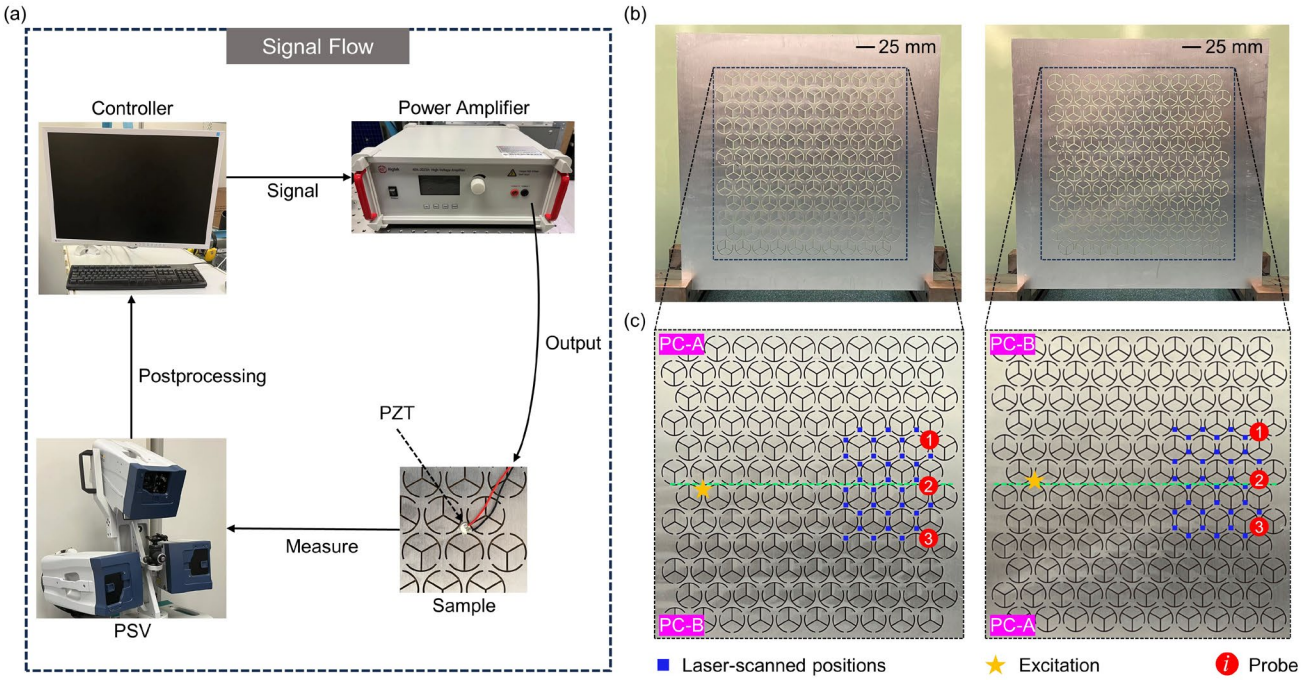

Fig. 6. (a) Experimental setups and the entire signal flow. (b) Samples with the interfaces Ψ_{AB} and Ψ_{BA}, respectively, where the lower left and lower right ends of the samples are clamped. (c) Detailed laser-scanned positions, excitation positions, and probe points for illustrative response spectra.

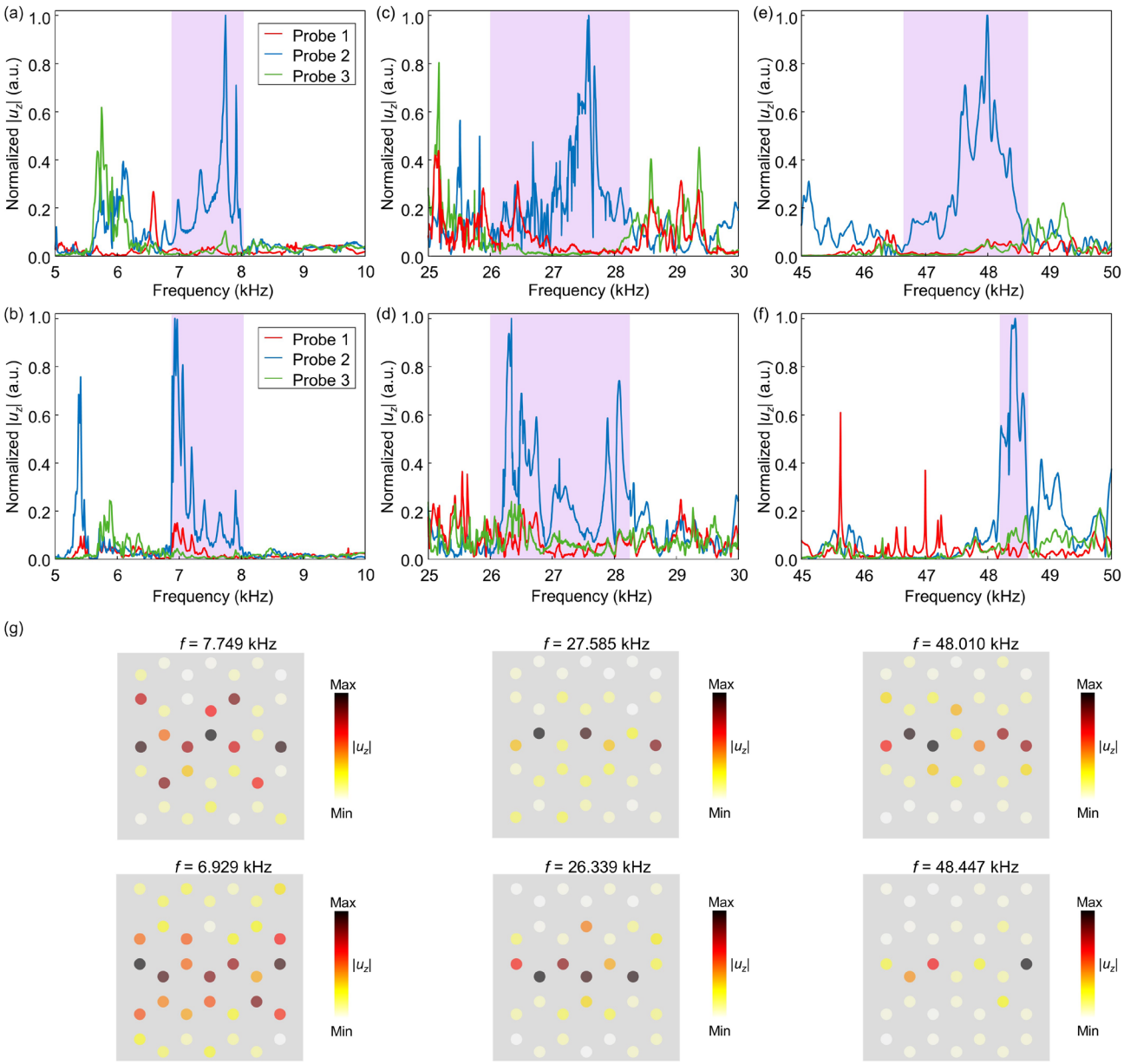

Fig. 7. Frequency spectra from the probes 1-3 on the plate with (a) Ψ_{AB} at frequencies 5-10 kHz, (b) Ψ_{BA} at frequencies 5-10 kHz, (c) Ψ_{AB} at frequencies 25-30 kHz, (d) Ψ_{BA} at frequencies 25-30 kHz, (e) Ψ_{AB} at frequencies 45-50 kHz, and (f) Ψ_{BA} at frequencies 45-50 kHz. Blue curves represent the responses of probe 2 while red and green curves represent the responses of probes 1 and 3, respectively. Shaded regions (pink color) refer to numerically predicted edge-state frequency ranges by supercell dispersions. (g) Experimentally measured displacement fields $|u_z|$ at corresponding peak frequencies in (a)-(f).

Specifically, the frequency response spectra extracted from the probes 1-3 (labeled in Fig. 6(c)) are picked up for further illustration. Clearly, the probe 2 located at the interface can acquire edge-state responses while the probes 1 and 3 detect bulk waves for comparison. Figures 7(a)-(f) illustrate the normalized responses of probes 1-3 on two plates around respective frequency ranges: 5-10 kHz for BG I, 25-30 kHz for BG II, and 45-50 kHz for BG III. We denote the numerically predicted frequency ranges of edge modes by pink shaded ribbons in Figs. 7(a)-(f), which locate at 6.875-8.056 kHz (Ψ_{AB} and Ψ_{BA} for BG I), 26.010-28.262 kHz (Ψ_{AB} and Ψ_{BA} for BG II), 46.646-48.617 kHz (Ψ_{AB} for BG III), and 48.185-48.617 kHz (Ψ_{BA} for BG III). As can be seen, around these frequencies, the responses at the edge probe 2 (blue curves) are very strong while the responses of bulk probes 1 and 3 (red and green curves) are relatively weak, as illustrated in Figs. 7(a)-(f). On the other hand, we extract the frequency domain signals of all scanned points [77,78] so as to visualize the wave fields. The wave fields at those peak frequencies of the response spectra of the probe 2 further verify that propagating waves are highly localized at the interfaces, as depicted in Fig. 7(g) Additionally, we also find that the gapped edge state within BG III for the interface Ψ_{BA} is well captured, reflected by differences between Fig 7(e) and Fig 7(f). Conclusively, despite minor frequency deviations due to several inevitable factors in experiments such as imperfectly fabricated samples and noise signals, the above findings confirm the fact that flexural waves are highly localized and transported along the interfaces, over those numerically predicted edge-state frequencies.

3.3 Robustness of edge-state propagation

Having demonstrated triband edge-state propagations of flexural waves along straight interfaces within BGs I-III, in the following, we evaluate the robustness of such

topological valley transports by examining their immunities against geometric perturbations including structural defects, disorders, and sharp bends in numerical simulations. For the cases analyzed here, the investigation on flexural-wave propagations along the interface Ψ_{AB} is used for an illustration. To simulate flexural wave propagations along the prescribed interface Ψ_{AB}, a phononic plate comprised of PC-A (up) and PC-B (down) is numerically established in the finite element software COMSOL Multiphysics 5.6. We use frequency response analysis in the 3D Solid Mechanics Modula of COMSOL Multiphysics to directly investigate flexural-wave propagation, in which the perfectly matched layers (PMLs) are available so that unwanted reflections from plate boundaries can be absorbed. In frequency domain simulations, an out-of-plane point force is applied at the entrance of the interfaces to excite flexural waves in plates, labeled by green stars in Fig. 8. In particular, we purposely introduce some geometric perturbations at the interfaces: a Z-shaped interface with two sharp bends, a defect by removing one unit-cell-scale slots, and a disordered area by rotating several slots with random θ values between [-5°, 5°] around their respective centers, as indicated in left panels of Fig. 8. The excitation frequencies are at those experimentally measured edge-state peak frequencies for the interface Ψ_{AB}. The resulting displacement fields $|u_z|$ show that, despite the existence of these geometric perturbations, flexural waves still propagate smoothly from the entrance to the exit of the interfaces with little energy loss, evidencing that tri-band valley edge modes are topologically robust.

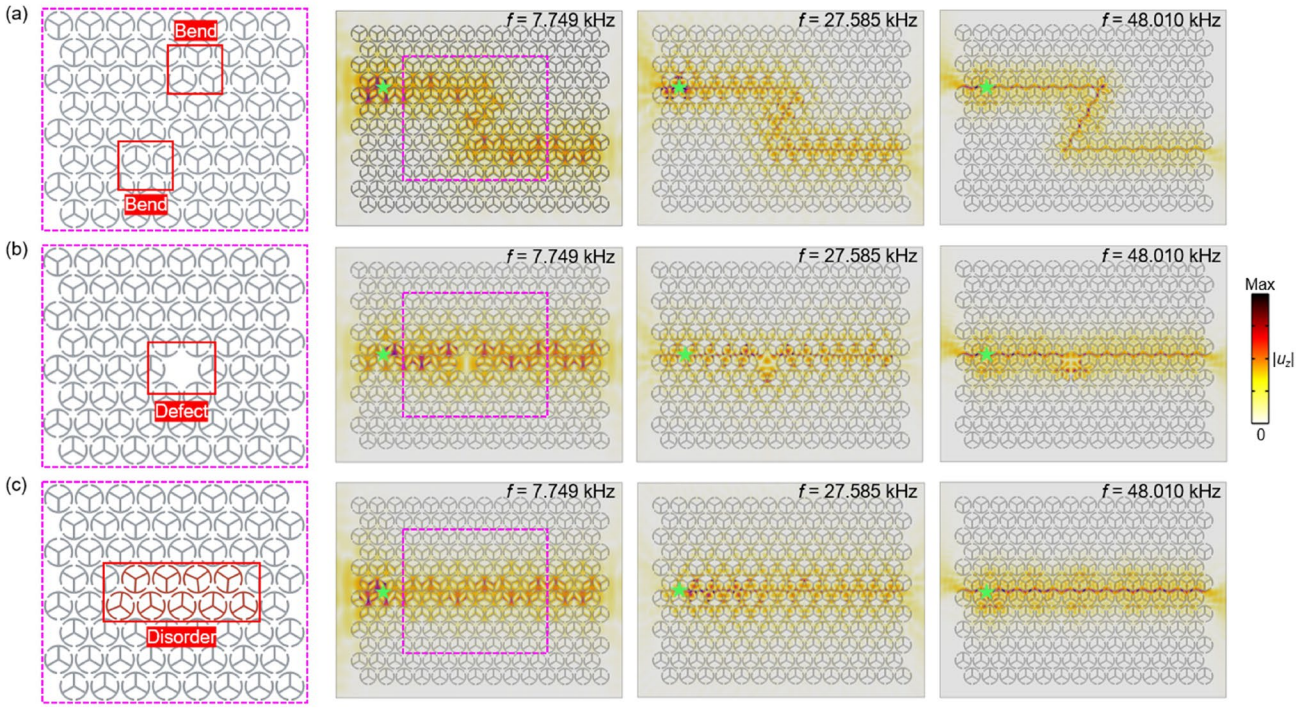

Fig. 8. Simulated displacement fields at peak frequencies (Fig. 7) in the phononic plate (Ψ_{AB}) with three types of geometric perturbations: (a) sharp bends (b) defects (c) disorders. Enlarged views of the regions boxed by purple-colored dashed lines are shown in the left panels, where red lines point out perturbations. Green colored stars mark positions of the excitation.

4. Second-order corner modes

Besides edge modes, valley Hall topological insulators have been proved to be capable of supporting zero-energy corner modes emerging from nontrivial bulk polarization [54,76]. The bulk polarization is a topological invariant that characterize a class of symmetry-protected topological phases, which reveals the appearance of higher-order topological states according to the locations of Wannier centers [79]. When valley edge modes are gapped in dispersions, nontrivial second-order corner modes can appear within the resulting edge gap and exhibit valley-selective characteristics [54,76]. In this section, we show that the proposed valley PTI hosts second-order topological corner

modes within those band gaps concerned.

4.1 Corner mode of Ψ_{BA} within BG III

It is noticed that the edge mode appearing at the interface Ψ_{BA} is gapped within BG III (Fig. 5(d)), providing the room for supporting the corner mode. To prove this, we construct a finite-sized plate (FP_1) comprising of PC-B surround by PC-A, where three 60-degree corners are formed between nearby interfaces Ψ_{BA}, as sketched by the inset in Fig. 9(a). Next, we calculate the eigenfrequencies of FP_1 to visualize the corner mode. Figure 9(a) shows that three degenerated corner mode (red dots) exactly occurs within the range of the edge gap, evidenced by the highly localized energy at the corner site, as seen in Fig. 9(c). For comparison, we build another finite-sized plate as the counterpart of FP_1, named as FP_2 (with reversed PC-A and PC-B) and see its eigenfrequencies. The results show that the edge modes of FP_2 are distributed across the entire BG III, but no corner mode exists, as depicted in Fig. 9(b).

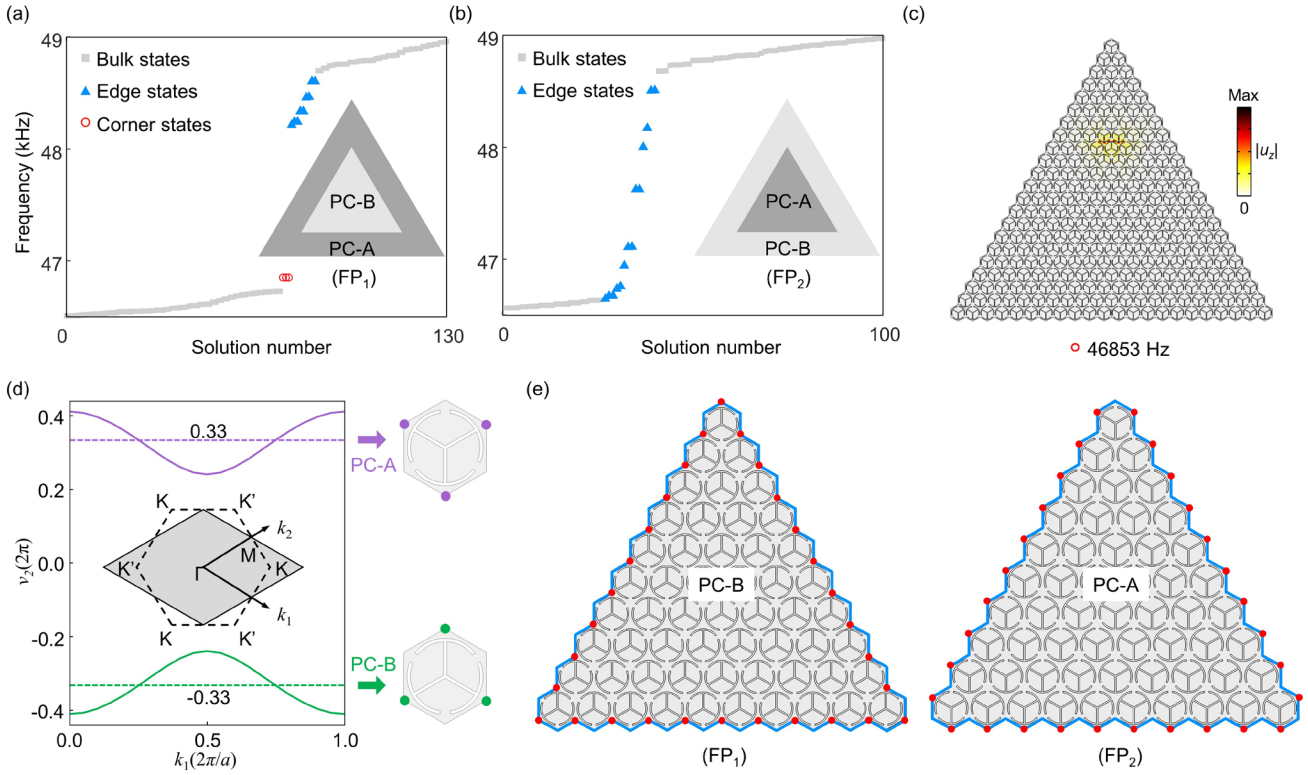

Fig. 9. (a)-(b) Eigenfrequencies around BG III for (a) FP_1 and (b) FP_2, where only bulk (gray dots), edge (blue dots) and corner mode (red dots) are presented while other irrelevant eigenmodes like ones at boundaries are unshown. The boundary conditions of FP_1 and FP_2 are set to be free in simulations. (c) Displacement field $|u_z|$ of corner-state eigenmode (red colored dot in (a)). (d) Wannier bands of PC-A and PC-B, where the inset shows the rhombus-shaped Brillouin zone for the calculation and dashed lines represent mean values of Wannier bands. The right panel shows that Wannier centers are located at Wyckoff positions. (e) Plotted Wannier centers (red dots) along interfaces (blue lines) of the inner domain of FP_1 and FP_2, respectively.

The underlying physics behind these findings can be elucidated by the second-order topology of PC-A and PC-B, characterized by the bulk polarizations, which can be numerically acquired using the Wilson-loop method [80]

$$P_\alpha = \frac{1}{2\pi}\int_L dv_{\alpha,k_\beta} \quad \alpha = 1, 2 \quad \beta = 2, 1 \tag{6}$$

where L represents the projected length of the adapted Brillouin zone (deformed from the hexagon to a rhombus, shown in the inset in Fig. 9(d)) along the k_β direction. v_{α,k_β} denotes Berry phase, the integration of Berry connection along a closed loop inside the Brillouin zone [71]. Here, it is integrated along the loop k_α for a specific k_β, which is expressed as

$$v_{\alpha,k_\beta} = \int_{-\pi}^{\pi} i\left\langle u_{m,\mathbf{k}}\left|\partial_{k_\alpha}\right|u_{m,\mathbf{k}}\right\rangle \mathrm{d}k_\alpha \tag{7}$$

where $|u_\mathbf{k}\rangle$ denotes the periodic wave functions of the m^{th} order band at wave vector $k = (k_\alpha, k_\beta)$. Figure 9(d) presents v_2 as a function of k_1 for PC-A and PC-B, respectively. According to Eq. (6), we can get $P_2 = 1/3$ for PC-A and $P_2 = -1/3$ for PC-B. Similar calculation on v_1 leads to $P_1 = P_2 = 1/3$ for PC-A and $P_1 = P_2 = -1/3$ for PC-B, indicating that Wannier centers are located at different Wyckoff positions for PC-A and PC-B, as

443 labelled by purple and green dots in the right panel of Fig. 9(d). So far, we know that
444 the bulk polarizations of PC-A and PC-B within BG III: P_A= (1/3, 1/3) while P_B= (−1/3,
445 −1/3) and then we label the Wannier centers in two finite-sized plates *i.e.*, FP_1 and FP_2,
446 which can determine the emergence of nontrivial corner modes. For convenience, only
447 those Wannier centers in the inner domain of each plate are labeled along the interfaces
448 while the entire outer domain is hidden. It is noticed that the Wannier centers along the
449 interfaces in FP_1 terminate at the corner position (as denoted by red circles in Fig. 9(e)),
450 implying that corner states occur at this corner site. On the contrary, the Wannier centers
451 disappear at the corner position in FP_2, meaning that the corner site cannot host corner
452 state. This reflects the so-called valley selectivity [54,76] and provides a physical insight
453 for understanding the difference between two types of interfaces, *i.e.*, Ψ_{BA} and Ψ_{AB}.
454
455 Having understood the physics of the second-order topology, we conduct a vibration
456 test to experimentally demonstrate the corner mode appearing in FP_1. A 6061-aluminum
457 alloy plate is fabricated by the laser cutting technology, the sizes of which are identical
458 with those of FP_1. Figure. 10(a) pictures the prepared specimen, where the position of
459 the excitation source (one PZT with 6 mm diameter and 1 mm thickness, placed at one
460 side of the plate) is displayed by a close view (the inset). Other experiment setups and
461 implementations are similar to those described in Section. 3.2. Here, we select one of
462 three identical corners for illustration, and the response spectrum (Fig. 10(c)) at this
463 corner position (red point on the specimen in Fig. 10(b)) shows that one response peak
464 appears at 46.465 kHz, which nearly coincides with the numerical one 46.853 kHz. The
465 slight frequency deviation is likely attributed to the differences between material
466 parameters of aluminum in the simulation

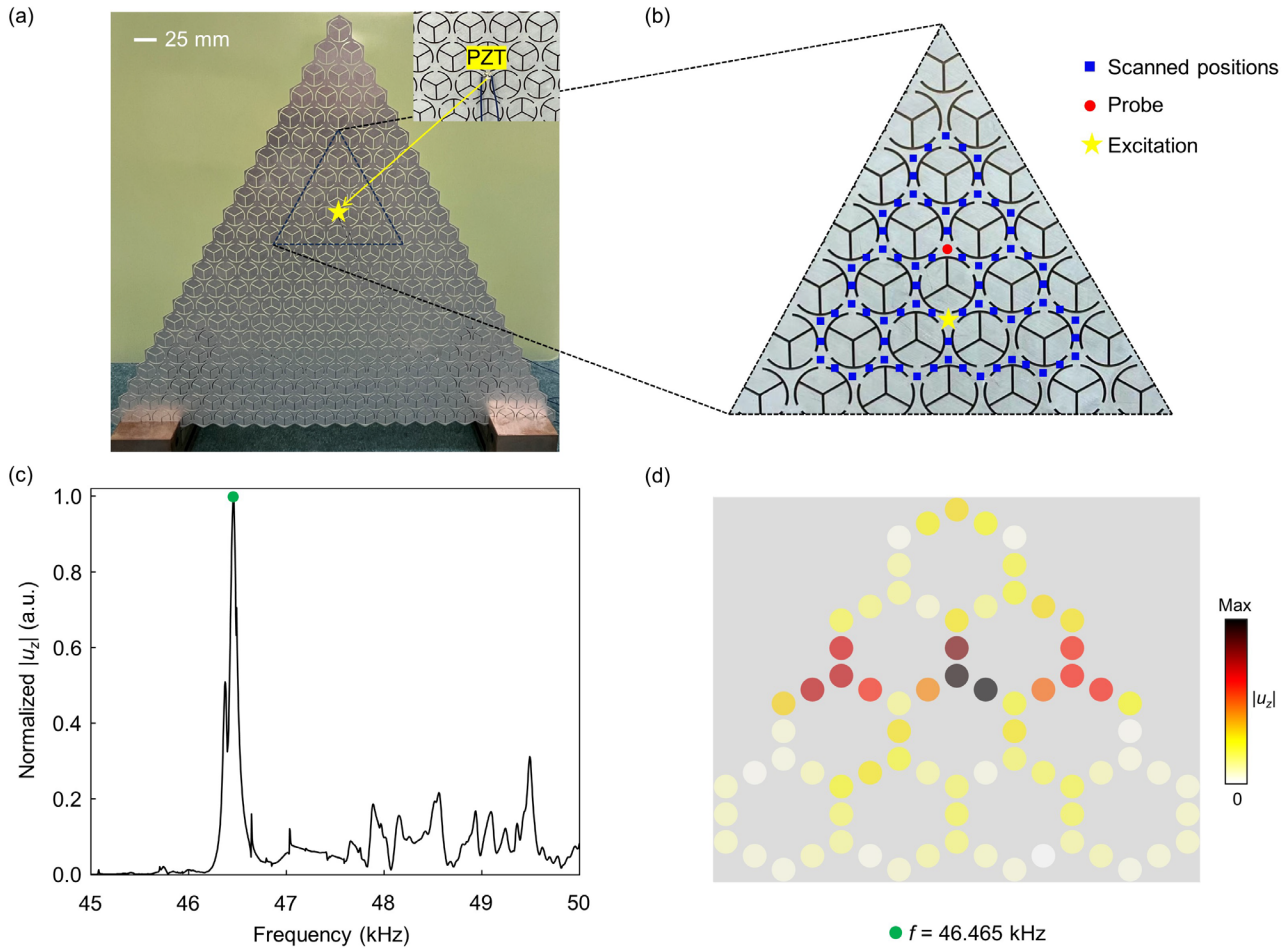

Fig. 10. (a) Experiment specimen for measuring the corner state, where the lower left and lower right ends of the sample are clamped. (b) Enlarged view of laser-scanned positions, the excitation position, and the probe point for extracting response spectrum. (c) Response spectrum at the probe point in (b). (d) Experimentally measured energy fields $|u_z|$ at the corresponding peak frequency in (c).

model and the actual specimen, and unavoidable manufacture error. Furthermore, the scanned energy field (Fig. 10(d)) around the corner site (see laser-scanned positions in Fig. 10(b)) at this peak frequency shows that energies are exactly confined at this corner position. So far, we have experimentally confirmed that the developed valley PTI in this paper is exactly a second-order topological insulator capable of hosting corner modes.

4.2 Topological corner modes within multiple band gaps

The previous section has verified the nontrivial second-order topology of the proposed valley PTI, but only within the third topological band gap. Theoretically, each topological band gap in valley PTIs can accommodate nontrivial corner modes, but that requires a gapped edge mode. As mentioned before, both interfaces Ψ_{AB} and Ψ_{BA} exhibit gapless edge modes within the first two topological band gaps, thereby uncapable of holding corner modes within BGs I-II. Instead, we utilize another pair of valley-contrast PCs, PC-C ($\theta = -15°$) and PC-D ($\theta = 15°$), to confirm the existence of multi-band corner modes in the proposed PTI.

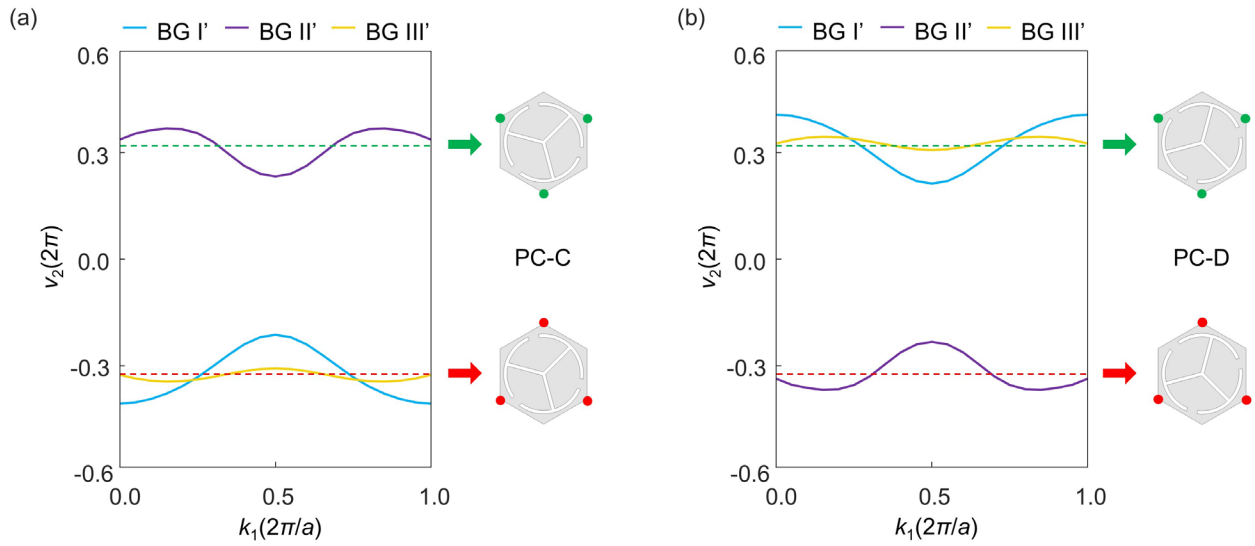

Fig. 11. (a)-(b) Wannier bands of the lower bands of BG I'-III' for (a) PC-C and (b) PC-D, where dotted lines denote mean values of Wannier bands. Red and green colored arrows show that Wannier centers are located at respective Wyckoff positions

First, in a similar way described in Section. 4.1, we calculate the Wannier centers of PC-C and PC-D within BGs I'-III'. Figure 11 presents Wannier bands along with positions

495 of resulting Wannier centers of PC-C and PC-D within three band gaps, by which one
496 can infer that multi-frequency corner modes occur when connecting PC-C and PC-D in
497 a manner similar to the one in Fig. 9. To investigate corner modes and their valley
498 selectivity, we build two finite-sized plates, *i.e.*, FP_3 and FP_4: FP_3 consists of PC-C
499 surrounded by PC-D, while FP_4 is made of PC-D surrounded by PC-C, as sketched at
500 the left panels in Figs. 12(a)-(b).
501
502 Subsequently, we calculate the eigenfrequencies of FP_3 and FP_4 around BGs I'-III', and
503 results are presented in Figs. 12(a)-(b). Notably, corner-state eigenmodes (red icons) are
504 discovered within those occurred edge gaps, evidenced by their highly localized
505 energies at corresponding corner sites, as depicted in Figs. 12(c)-(d). According to the
506 positions of Wannier centers, some of corner modes are distinguished as topologically
507 nontrivial corner states (red dots) while others are just trivial ones (red diamonds): For
508 FP_3, the Wannier centers in its inner layer terminate at the corner position within BG I'
509 and BG III' while disappears at the corner position within BG II'. This further reflects
510 the fact that no corner mode exists within BG II' for the FP_3, as depicted in Fig. 12(a).
511 While for FP_4, the Wannier centers terminate at the corner position only within BG II'.
512 Therefore, even though corner modes are discovered within BG I' and BG III' of FP_4,
513 they should be classified as trivial ones [52].
514
515 Next, we fabricate these two finite-sized plates, *i.e.*, FP_3 and FP_4, to experimentally
516 observe these numerically predicted corner modes. The whole experiment follows the
517 same procedures as those in Section. 4.1. For both plates, the measured response spectra
518 around corner-state frequencies are sequentially displayed in Figs. 13(a)-(b). It should

519 be particularly stressed that the illustrated response spectra are not always extracted at
520 the actual corner position, instead they are extracted at positions with maximal energy
521 amplitude in the experimentally scanned energy fields. For each corner mode, it can be
522 seen that the experimentally measured response peak is close to the numerical result.
523 The reasons for occurred frequency deviations between numerical and experimental
524 results have been given in Section. 4.1. Specially, two neighboring corner modes within
525 BG III' (for both FP_3 and FP_4) are also well captured, which are reflected by two close
526 peaks in the measured response spectra, as seen in Figs. 13(a)-(b). Moreover, at all these
527 response peaks, the highly-localized energy fields scanned around corner sites reinforce
528 the fact that they represent topological corner modes, as displayed in Figs. 13(c)-(d). It
529 can be seen that the experimentally scanned corner-state energy fields exhibit diverse
530 localizations around the corner position, showing good consistency with corner-state
531 eigenfields in numerical simulations in Figs. 12(c)-(d).
532
533 The above investigation has verified the emergence of valley-selective corner modes
534 within all three topological band gaps, demonstrating that the proposed PTI is also a
535 second-order topological insulator capable of accommodating multi-band corner states.
536 The robustness of topological corner modes is verified in Appendix. C.
537

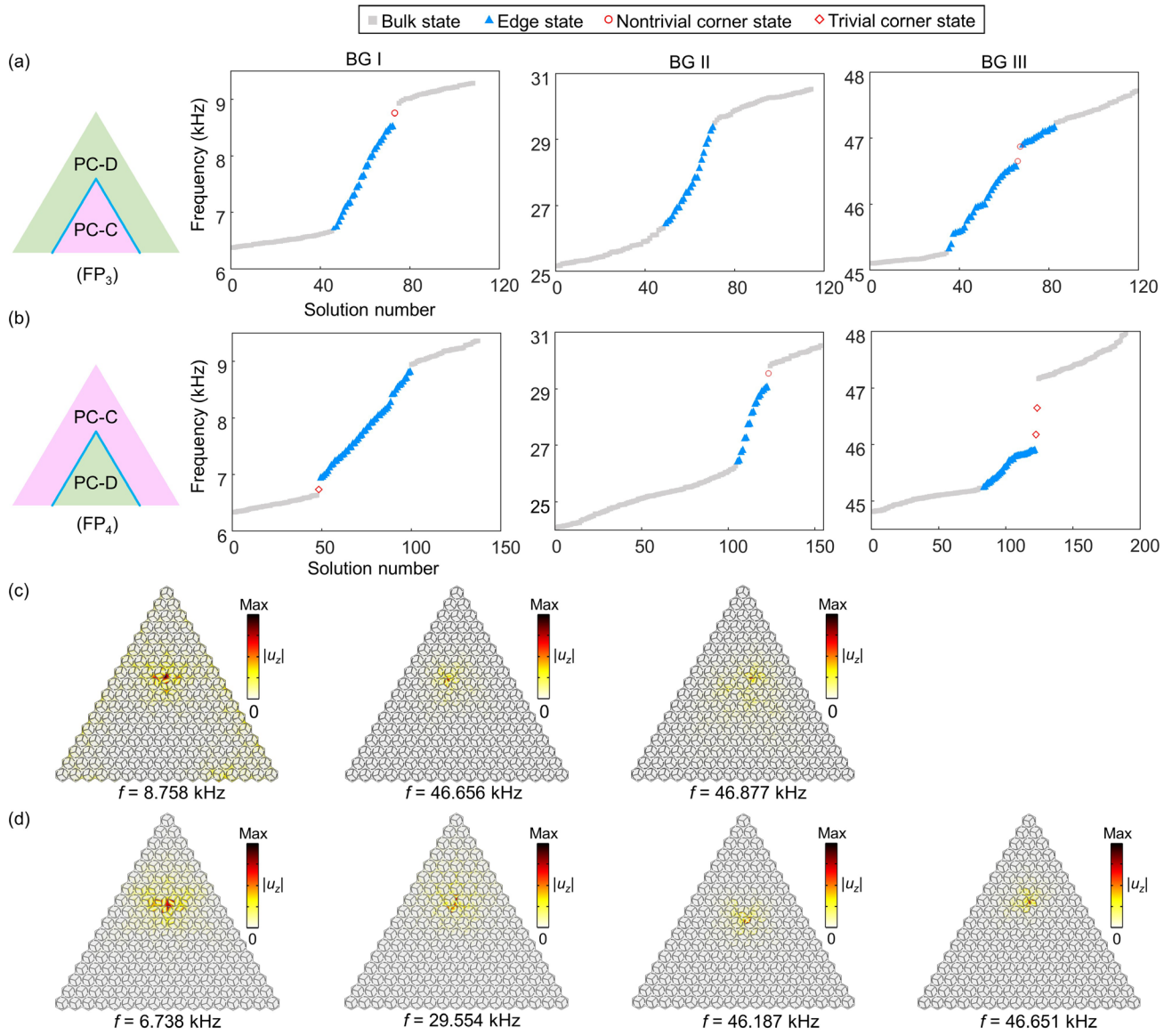

Fig. 12. (a)-(b) Eigenfrequencies of finite-sized plates (a) FP_3 and (b) FP_4 around frequencies of BGs I'-III'. (c)-(d) Eigenfields of the corner modes labeled in (a)-(b). Boundary conditions of these finite-sized plates are set to be free in simulations.

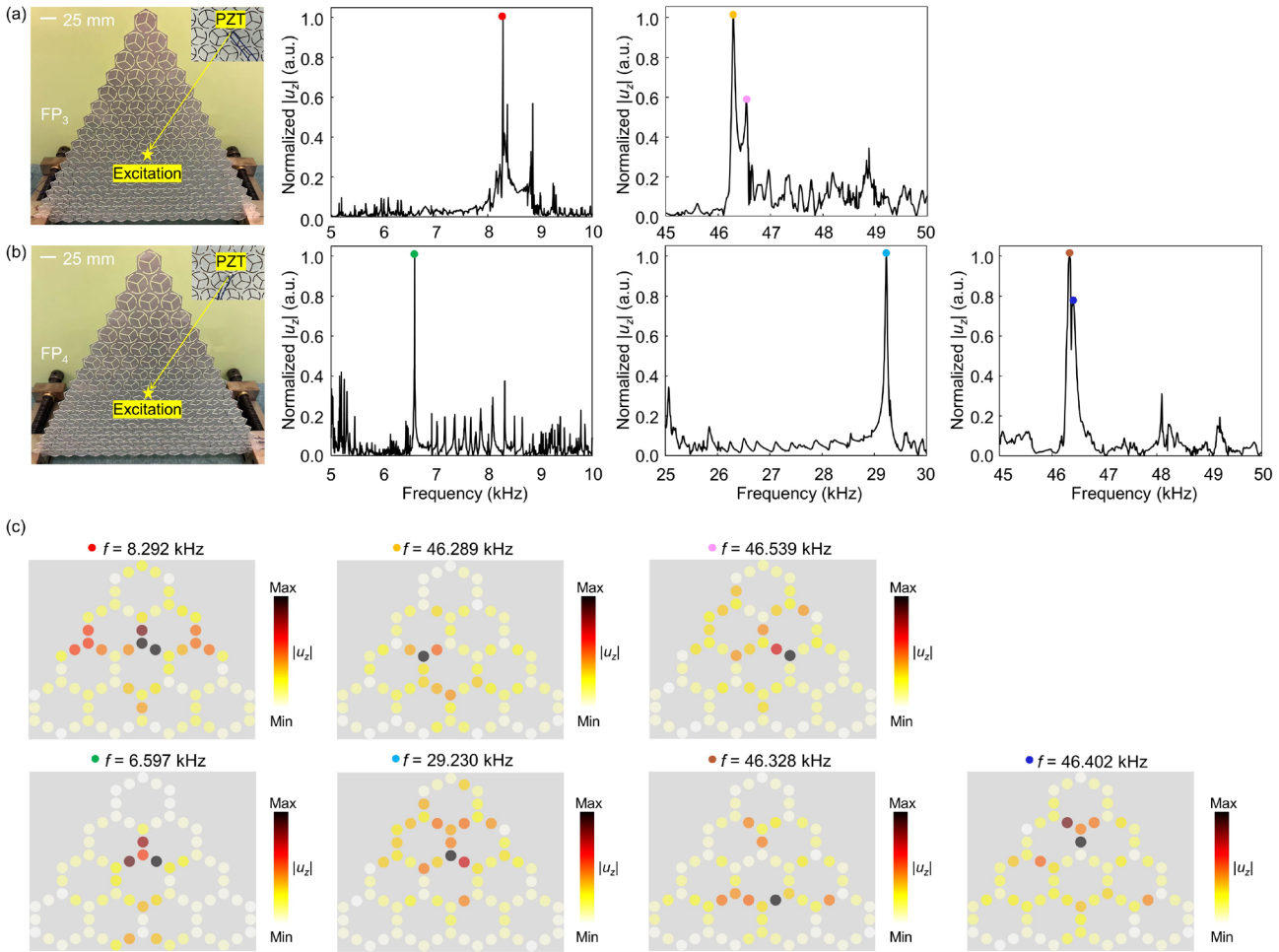

Fig. 13. (a) Fabricated FP_3 and the response spectra within BG I' and III'. (b) Fabricated FP_4 and the response spectra within BG I', BG II', and BG III'. In (a) and (b), the lower left and lower right ends of the samples are clamped. (c) Experimentally scanned displacement fields $|u_z|$ at the corresponding peak frequencies at the spectra in (a)-(b).

5. Parametric studies

To highlight the applicability of our design strategy for multi-band PTIs in general plate-type structures, parametric studies are performed in this part. Rather than focusing on the widths of topological band gaps that are highly sensitive to the orientation angle θ (referring to Fig. 3), we here consider the effects of slots parameters and the plate thickness on the emergence of those multi-frequency valley-shaped Dirac degeneracy bands when $\theta = 0°$. It is important to stress that degeneracies often occur at K (K') points due to the C_{3v} symmetry, but they are not necessarily able to open a complete band gap. Particularly, the valley-shaped degeneracy bands play a critical role in enabling complete band gaps. In previous works that leverage perforations in plates for creating Dirac degeneracy, the sizes of holes and distance among them need to be strictly controlled to produce effective valley-shaped degeneracy bands. In other words, the effective Dirac cone is very sensitive to the sizes of perforated holes. Here, we demonstrate that the emergence of valley-shaped degeneracy bands in the proposed PTI perforated with SRRs are insensitive to geometric parameters, broadening its applicability in general plate-type structures. Moreover, we show that more Dirac cones emerge at other dispersion branches, besides the three previously studied. All numerical calculations still employ plate models except the effect of thickness h, which is implemented by the 3D Solid Mechanics Module in COMSOL 5.6.

5.1 Effects of geometric parameters on degeneracy bands

We investigate the effects of changing geometric parameters on three pairs of degeneracy bands, referring to the 7^{th} and 8^{th}, the 13^{th} and 14^{th}, and the 19^{th} and 20^{th} bands. Accordingly, we refer three concerned degeneracy points as the degeneracy I-III.

Figures 14-17 present dispersion bands around frequencies of three pairs of degeneracies when continuously changing the rib width *e* (Fig. 14), the slot width *t* (Fig. 15), the plate thickness *h* (Fig. 16), and the outer radius *r* (Fig. 17). Clearly, even though changes of parameters *e*, *t*, and *h* cause frequency shifts of these degeneracies, relevant degeneracy bands maintain valley-shaped, which are further proved to smoothly open complete band gaps and cause topological phase transitions. However, when continuously reducing the outer radius *r* of slots, although degeneracies still exist, it can be seen that associated degeneracy bands are severely disrupted such as distorted line shapes or intersection with other branches, as indicated in Fig. 17. On this condition, we assert that the valley shapes of degeneracy bands are broken, and these degeneracies become ineffective Dirac cones uncapable of opening complete band gaps.

The phenomena can be further elucidated by the underlying mechanism on the formation of these degeneracy bands, that is, the resonances of perforated SRRs have a significant impact on the dispersion: the changes to parameters *e*, *t*, *h* certainly affect resonant frequencies, but have little effect on the relative mass ratio of perforated SRRs to the host plate. While the outer radius *r* is smaller, perforated SRRs have a less relative mass so that dispersion curves are seriously disrupted. Detailed discussion can be found in Appendix B.

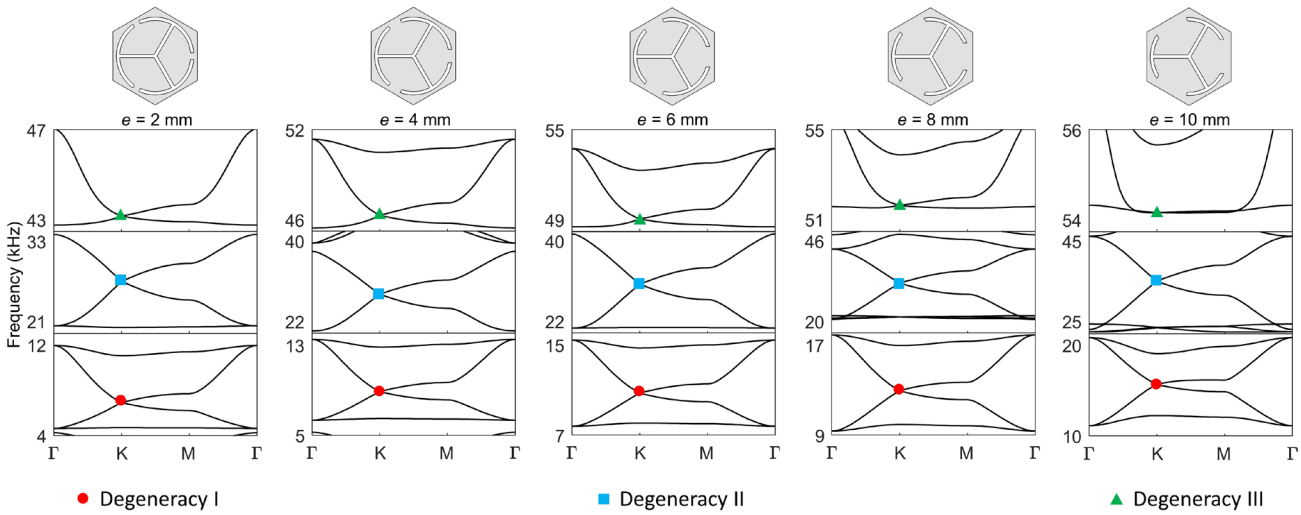

Fig. 14. Evolutions of three pairs of degeneracy bands when changing the rib width e from 2 mm to 10 mm, where the degeneracy I-III are labeled by colored signs, located between the 7th and 8th bands, the 13th and 14th bands, and the 19th and 20th bands, respectively.

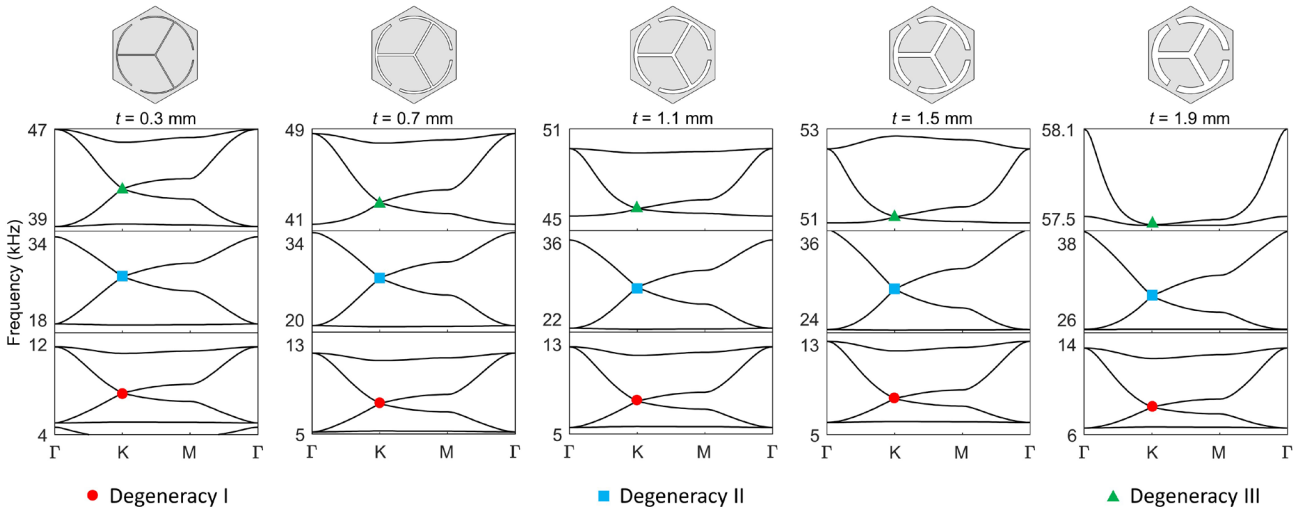

Fig. 15. Evolutions of three pairs of degeneracy bands when changing the slot width e from 0.3 mm to 1.9 mm, where the degeneracy I-III are labeled by colored signs, located between the 7th and 8th bands, the 13th and 14th bands, and the 19th and 20th bands, respectively.

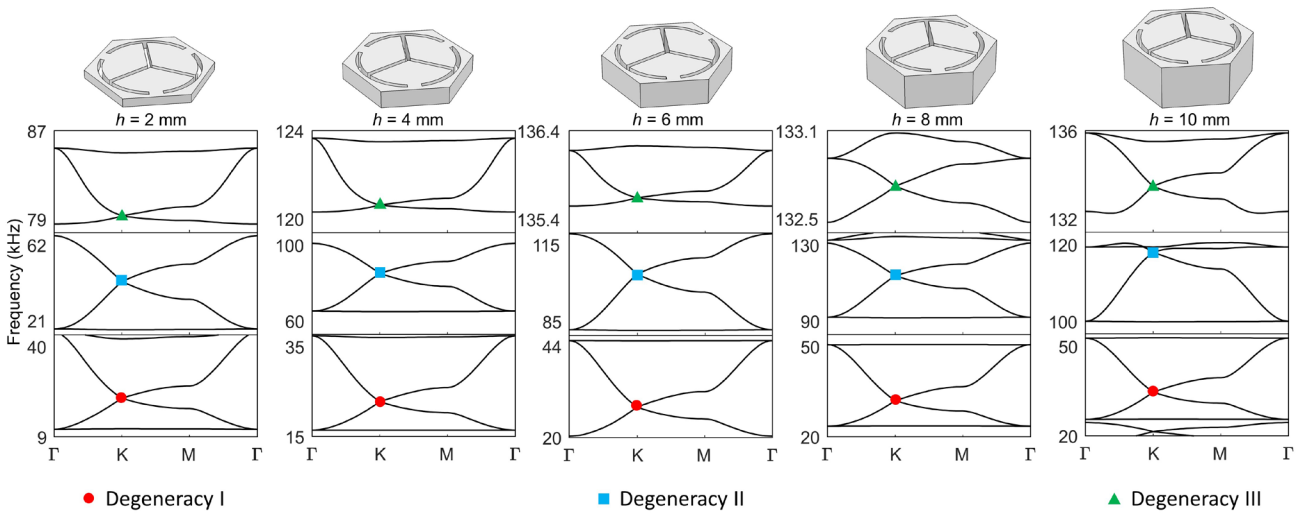

603

604 Fig. 16. Evolutions of three pairs of degeneracy bands when changing the plate thickness h from 2 mm to 10

605 mm, where the degeneracy I-III are labeled by colored signs, located between the 7th and 8th bands, the 13th

606 and 14th bands, and the 19th and 20th bands, respectively.

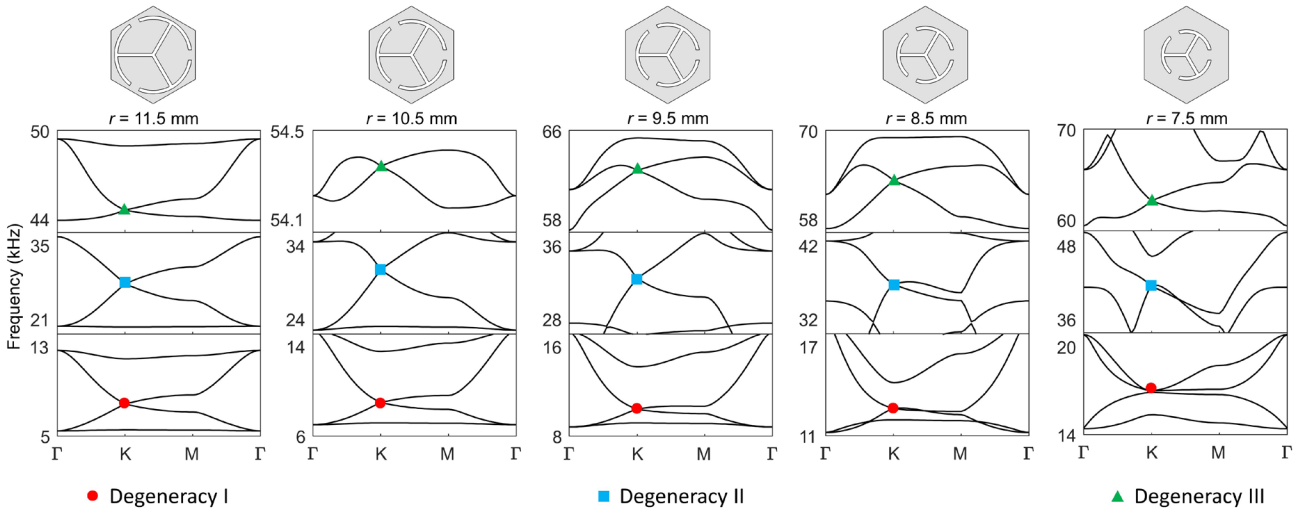

607

608 Fig. 17. Evolutions of three pairs of degeneracy bands when changing the outer radius r from 11.5 mm to 7.5

609 mm, where the degeneracy I-III are labeled by colored signs, located between the 7th and 8th bands, the 13th and

610 14th bands, and the 19th and 20th bands, respectively.

611

612 The above parametric studies show that the existence and the valley shapes of multiple

613 Dirac degeneracy bands are not accidental results through fine-tuning the sizes of

perforated holes, but due to the existence of SRRs. Correspondingly, provided that perforated SRRs remain a large relative mass, these Dirac cones persist. This demonstrates the generality of our strategy, which is applicable to both thin and thick plates. The developed perforation fashion in this paper, referring to perforating SRRs by thin slots, offers a promising solution to the challenge of designing multi-band PTIs in plain plate structures without attaching or embedding complex scatterers.

5.2 Dirac degeneracies at additional dispersion bands

The investigations in Section. 5.1 still focus on those degeneracies that locate between the 7^{th} and 8^{th}, the 13^{th} and 14^{th}, and the 19^{th} and 20^{th} bands. In the following, we show that the proposed phononic plate allows for additional Dirac cones at other dispersion branches, not limited to the previously analyzed three.

Besides the first twenty-one dispersion bands calculated in previous cases, we here consider dispersion bands at higher frequencies. Figure 18(a) shows the 25^{th}-30^{th} dispersion bands when $\theta = 0°$, where two valley-shaped degeneracies at K points are identified between the 25^{th} and 26^{th}, and the 28^{th} and 29^{th} bands. Further, these two degeneracies are lifted up to open complete band gaps when rotating a small angle θ by -5°, and each pair of K valleys carry opposite OAMs, as shown in Fig. 18(b). Therefore, these two degeneracies are also effective Dirac cones, referred as Dirac cones IV and V.

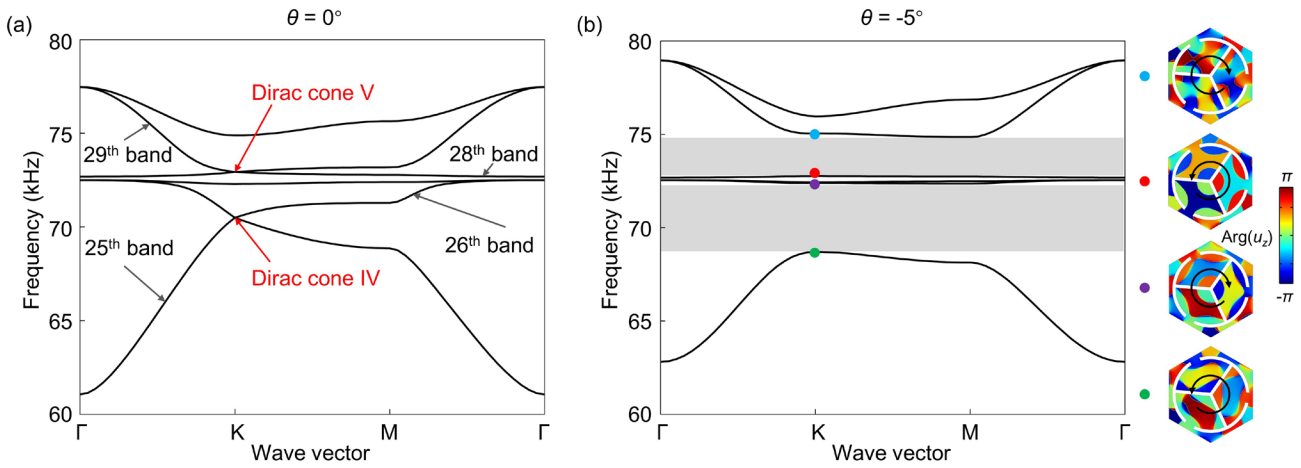

634

635 Fig. 18. (a) The 25th – 30th dispersion bands of the unit cell when $\theta = 0°$. Dirac cone IV is located between the
636 (25th, 26th) while Dirac cone V is located between the (28th, 29th). (b) The 25th – 30th dispersion bands of the unit
637 cell when $\theta = -5°$. Right panel in (b) depicts phase fields of u_z at those colored dots. Gray shaded regions
638 represent the complete band gaps.

639

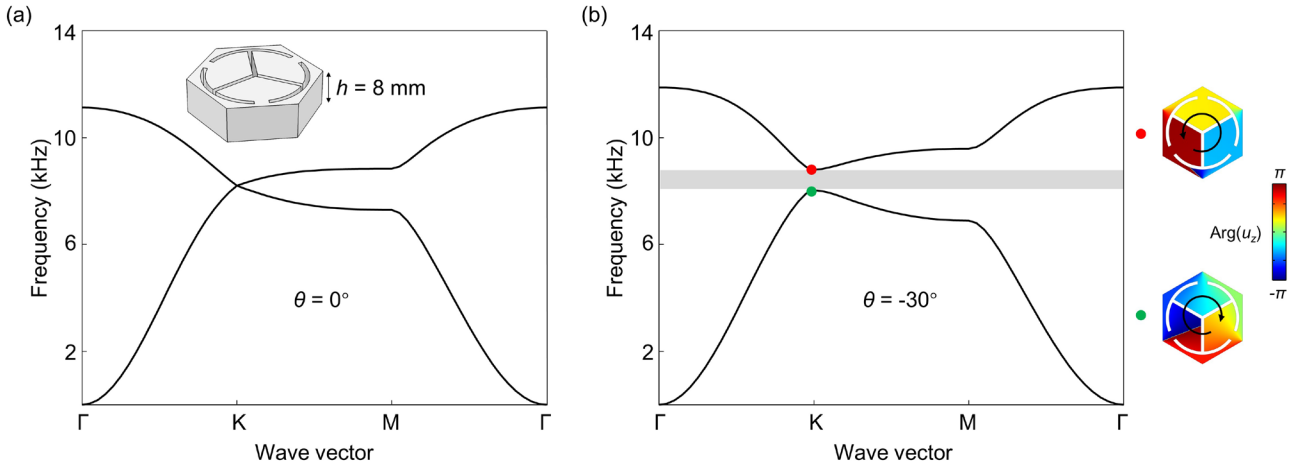

640

641 Fig. 19. The 1st and 2nd dispersion bands of the unit cell with thickness $h = 8$ mm when (a) $\theta = 0°$ (b) $\theta = -30°$.
642 Right panel in (b) depicts phase fields of u_z at those colored dots. Gray shaded region represents the complete
643 band gap.

644

645 Next, we demonstrate that several degeneracies at K points, which are previously
646 considered as ineffective Dirac cones, can become effective ones with specific

parameters. Figure 1(c) shows that the 1st and 2nd dispersion bands are degenerated at K points, but these two bands are not with perfectly valley-shaped and uncapable of opening a complete band gap via rotating orientation angle θ. However, the situation has changed with specific geometric parameters, *e.g.*, the thickness of the unit cell is set to be 8 mm with other parameters unchanged. Figures 19(a)-(b) present the 1st and 2nd dispersion branches of the new unit cell when $\theta = 0°$ and $\theta = -30°$, respectively. It can be seen that two degeneracy bands now exhibit perfect valley shapes when $\theta = 0°$, and successfully open a complete band gap carrying opposite OAMs at upper and lower K valleys, when θ is rotated to -30°. Based on this, we can identify that the degeneracy between the 1st and 2nd bands has become a new Dirac cone when the plate thickness h = 8 mm.

The above examples have demonstrated the extraordinary ability of our phononic plate to trigger multi-band Dirac degeneracies and its flexibility in parametric designs, not limited to the three previously studied.

6. Conclusions

In summary, we have developed a new type of micro-perforated elastic phononic plates, and on this platform, we successfully create multi-band valley PTIs with the ease of implementation and fabrication. The rich multi-modal resonances of perforated fan-shaped SRRs with C_3 symmetry induce effective Dirac cones in flexural-wave dispersions at different frequencies, which lead to multi-frequency complete topological band gaps. When rotating perforated slots properly, the topological phase transitions

occur within triple band gaps and two valley-contrast nontrivial PCs can be built.

The multi-band energy localization and robust propagation of flexural waves at the interfaces that connect two valley-contrast PCs have been demonstrated numerically and experimentally. Furthermore, these band gaps have been proved capable of accommodating second-order topological corner modes that originate from their nontrivial bulk polarizations, enriching topological physics of the developed PTIs. Experimental measurements validate their highly-localized energies around corner sites, facilitating applications of confining and amplifying multi-frequency elastic waves.

Parametric studies reveal that, the emergence of valley-shaped Dirac degeneracy bands in the proposed PTI is insensitive to the plate thickness and most slots parameters, reflecting its wide applicability in plate-type structures. Additional Dirac cones are discovered at higher frequencies, not limit to the three concerned. Moreover, with specific geometric parameters, several previously ineffective degeneracies at K/K' points become new Dirac cones capable of opening topological complete band gaps.

The proposed design strategy for realizing multi-band valley modes of flexural waves is universal, and applicable to almost all thin and thick plate-type structures constituted by various solid materials. This simple and flexible platform, created by easily achievable laser cutting or water jetting technologies, greatly facilitates to observe and leverage multi-band topological effects of elastic waves in practice.

Appendix A. Comparison between plate and solid models

In this appendix section, we compare the band structures calculated by the plate model with the one by three-dimensional FE model. The upper panel of Fig. A1(a) presents mesh geometry of the plate model used in this paper while the lower panel illustrates its solid counterpart with a finer mesh size. In Fig. A1(b), it can be seen that the dispersion of out-of-plane modes of the solid model (overlapped black dots with green curves) almost agree with curves of the plate model, despite of sparser meshes adopted in the latter. The above comparison validates the accuracy of the plate model used in this paper.

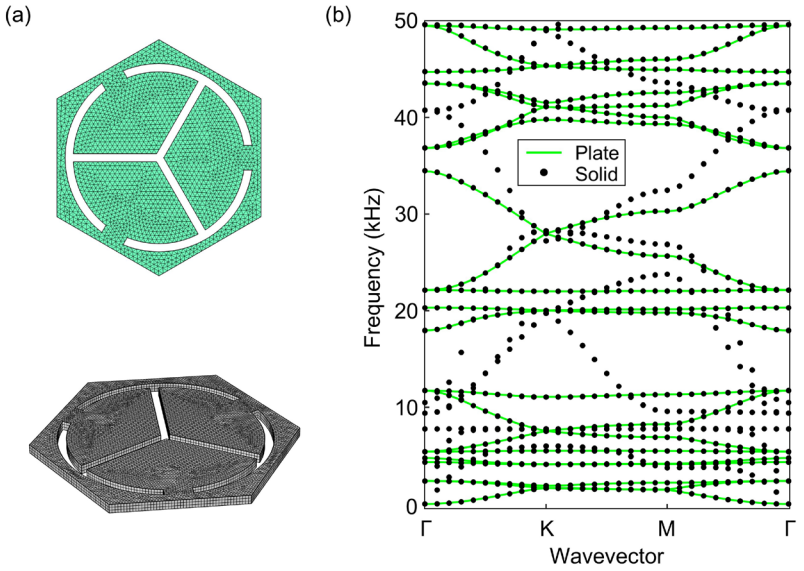

Fig. A1. (a) Mesh geometries of two-dimensional (2D) plate used in this paper (upper panel) and three-dimensional (3D) solid (lower panel). (b) Comparison of band structures calculated by two models, where overlapped dispersions refer to out-of-plane modes.

Appendix B. Mechanism analysis on multiple Dirac degeneracy bands

In this section, we discuss the mechanism underpinning the formation of those multiple Dirac degeneracy bands. Bloch eigenmodes at degenerated K valleys offer the insight for the underlying modal information. In the phononic plate, micro-perforated slots in fact carve out a type of fan-shaped SRRs moving like cantilevers, which are connected with the host plate via the ribs. In this situation, the total mass of three SRRs is much larger than the one of the host plate so that the resonances of the former play a dominative role in shaping flexural-wave dispersions. Figure A2 shows Bloch eigenmodes at Dirac cones I-III: Dirac cone I is induced by the torsional motions of SRRs, while Dirac II and Dirac III are the outcomes of the multi-modal bending resonances of SRRs. This fundamentally distinguishes from other existing perforation fashions that require strict hole sizes or distances among them to create the effective valley-shaped degeneracies. Particularly, in our PTI, the intrinsic C_3 symmetry of slots result in degeneracies at K/K' points while the special multi-order resonant modes of perforated SRRs make these degeneracies available as effective Dirac cones. These assertions are also confirmed in parametric studies in Section. 5: the changes to the rib width e, the slots width t, and the plate thickness h, only affect resonant frequencies but have little to no impact on the emergence and the valley shape of degeneracy bands because the relative mass of SRRs to the host plate are almost unchanged. While a smaller outer radius r of the slots leads to less relative mass of perforated SRRs, and thus their resonances cause weaker effects on dispersions, consequently disrupting the degeneracy bands, as shown in Fig. 17.

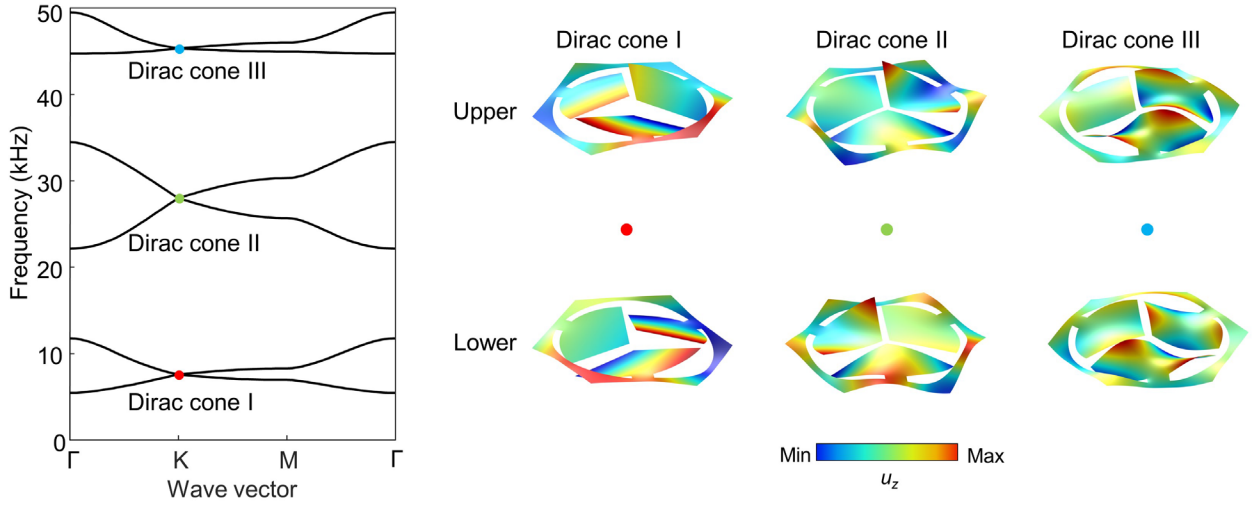

Fig. A2. Eigenfields at upper and lower K valleys of three concerned Dirac cones. The right panel shows the resonant deformation of these eigenmodes, where the colors represent out-of-plane displacement.

Appendix C. Robustness of corner modes

The inherent nontrivial topological property endows the corner modes with robustness against geometric perturbation such as structural defects. To prove this, we select FP_3 that hosts dual-band corner modes within BG I' and BG III' for illustration, and introduce a big defect by removing one unit-cell-scale slot close to the corner position. The calculated eigenfields show that the highly-localized corner modes are still observed despite slight frequency deviations, as seen in Fig. A3. In fact, corner modes, especially for their occurrence frequencies, have been revealed to maintain strong robustness to geometric perturbation in the bulk yet still be sensitive to perturbation close to the actual corner position [54,81]. Based on a modest frequency shift (<1%) induced by a big defect close to the corner position, the corner modes in the proposed PTI still exhibit robustness to a certain extent. On the other hand, the sensitivity to near-field perturbation might be leveraged for tunable wave localization.

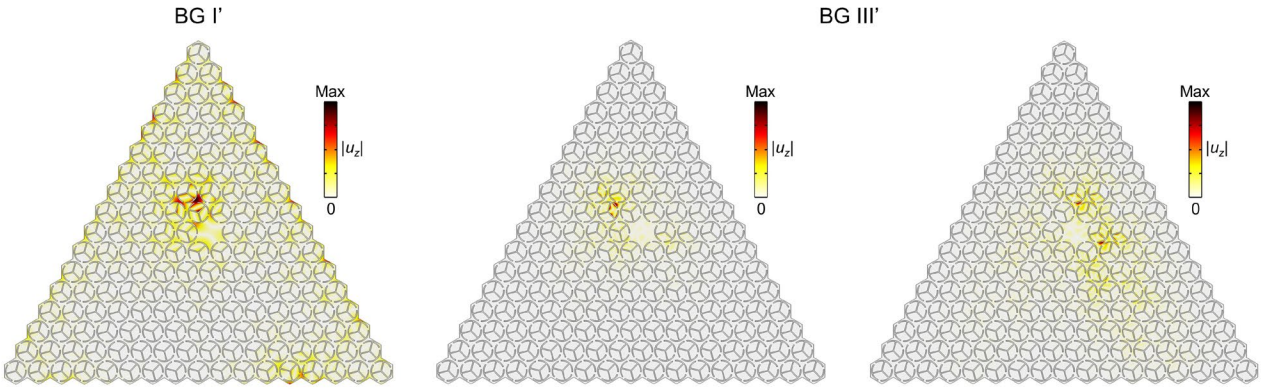

Fig. A3. Eigenfields $|u_z|$ of corner modes in the defected FP_3. The defect is created by removing a unit-cell-scale slot. The boundary conditions of the plate are set to be free in simulations.

Acknowledgement

This work is supported by the National Natural Science Foundation of China (No. 1210020421, 92263208), the Natural Science Foundation of Hunan Province (2022JJ40026), the Fundamental Research Funds for the Central Universities, the Research Grants Council of Hong Kong SAR (Nos. 15200922, 15202820, 15204419 and AoE/P-502/20).

References

[1] X.-L. Qi, S.-C. Zhang, Topological insulators and superconductors. Rev Modern Phys, **83**(4) 1057 (2011).

[2] L. Lu, J. D. Joannopoulos, and M. Soljačić, Topological photonics. Nat. Photonics, **8**(11), 821-829 (2014).

[3] J. Lu, C. Qiu, S. Xu, Y. Ye, M. Ke, Z. Liu, Dirac cones in two-dimensional artificial crystals for

762 classical waves. Phys. Rev. B, **89** (13) 134302 (2014)
763 [4] X. Li, S. Yu, H. Liu, M. Lu, and Y. Chen, Topological mechanical metamaterials: A brief review,
764 Curr. Opin. Solid State Mater. Sci. **24** 100853 (2020).
765 [5] H. Huang, J. Chen, and S. Huo, Recent advances in topological elastic metamaterials, J. Phys.:
766 Condens. Matter **33**, 503002 (2021).
767 [6] C. He, X. Ni, H. Ge, X.-C. Sun, Y.-B. Chen, M.-H. Lu, X.-P. Liu, Y.-F. Chen, Acoustic topological
768 insulator and robust one-way sound transport. Nat. Phys, **12** (12) 1124-1129 (2016)
769 [7] C. Lu, C. Wang, M. Xiao, Z. Q. Zhang, & C. T. Chan, Topological rainbow concentrator based on
770 synthetic dimension. Phys. Rev. Lett. **126**(11), 113902 (2021).
771 [8] X.-L. Tang, T. -X. Ma, and Y. -S. Wang, Topological rainbow trapping and acoustic energy
772 amplification in two-dimensional gradient phononic crystals. Appl. Phys. Lett. **122** 112201 (2023).
773 [9] M. Miniaci, R. K. Pal, R. Manna, and M. Ruzzene, Valley-based splitting of topologically protected
774 helical waves in elastic plates, Phys. Rev. B **100**, 024304 (2019).
775 [10] M. Oudich, N. J. Gerard, Y. Deng, and Y. Jing, Tailoring structure-borne sound through bandgap
776 engineering in phononic crystals and metamaterials: A comprehensive review, Adv. Funct. Mater. **33**,
777 2206309 (2023).
778 [11] R. Süsstrunk, S.D. Huber, Observation of phononic helical edge states in a mechanical topological
779 insulator. Science, **349** (6243) 47-50 (2015)
780 [12] H. Chen, H. Nassar, G.L. Huang, A study of topological effects in 1D and 2D mechanical lattices,
781 J Mech Phys Solids, **117** 22-36 (2018)
782 [13] S.H. Mousavi, A.B. Khanikaev, Z. Wang, Topologically protected elastic waves in phononic
783 metamaterials, Nat Commun, **6**, 8682 (2015)
784 [14] Z. Chen, Y. Wu. Tunable Topological Phononic Crystals, Phys. Rev. Applied **5**, 054021 (2016)
785 [15] H. Ren, T. Shah, H. Pfeifer, C. Brendel, V. Peano, F. Marquardt, and O. Painter, Topological

786 phonon transport in an optomechanical system, Nat. Commun. **13**, 3476 (2022).
787 [16] P. Wang, L. Lu, K. Bertoldi, Topological phononic crystals with one-way elastic edge waves, Phys.
788 Rev. Lett, **115**, 104302 (2015)
789 [17] H. Chen, L. Y. Yao, H. Nassar, and G. L. Huang, Mechanical Quantum Hall Effect in Time-
790 Modulated Elastic Materials, Phys. Rev. Appl. **11**, 044029 (2019).
791 [18] L. Fu. Topological crystalline insulators. Phys. Rev. Lett. **106** 106802 (2011).
792 [19] T.-W. Liu, F. Semperlotti, Tunable acoustic valley-hall edge states in reconfigurable phononic
793 elastic waveguides. Phys. Rev. A, **9** (1), 014001 (2018)
794 [20] J. Wang, J. Mei, Topological valley-chiral edge states of Lamb waves in elastic thin plates. Appl
795 Phys Express, **11** (5), 057302 (2018)
796 [21] Z. Zheng, J. Yin, J. Wen, D. Yu, & X. Chen. Switchable corner states in phononic crystals realized
797 by inverse design. Int. J. Mech. Sci. **243**, 108035 (2023)
798 [22] C. Brendel, V. Peano, O. Painter, F. Marquardt, Snowflake phononic topological insulator at the
799 nanoscale. Phys. Rev. B, **97** (2), 020102 (2018)
800 [23] Y. Chen, J. Li, and J. Zhu, Topology optimization of quantum spin Hall effect-based second-order
801 phononic topological insulator, Mech. Syst. Signal Process. **164**, 108243 (2022).
802 [24] D. Jia, Y. Wang, Y. Ge, S.-Q. Yuan, H.-X. Sun, Tunable Topological Refractions in Valley Sonic
803 Crystals with Triple Valley Hall Phase Transitions. Prog Electromagn Res **172**:13–22 (2021)
804 [25] D. Jia, Y. Ge, H. Xue, S. Yuan, H. Sun, Y. Yang, X. Liu, and B. Zhang, Topological refraction in
805 dual-band valley sonic crystals, Phys. Rev. B **103**, 144309 (2021)
806 [26] Z. Huang, J. Wu, Y. Lei, C. Liu, F. Ma, Multi-band acoustic topological insulator, Mater. Today
807 Phys. **27**,100793 (2022)
808 [27] E.J.P. Miranda, E.D. Nobrega, A.H.R. Ferreira, J.M.C. Dos Santos, Flexural wave band gaps in a
809 multi-resonator elastic metamaterial plate using Kirchhoff-Love theory, Mech. Syst. Signal Process.

116, 480-504 (2019).

[28] S.A. Cummer, J. Christensen, A. Alù. Controlling sound with acoustic metamaterials. Nat. Rev. Mater., **1**, 16001 (2016)

[29] R. K. Pal and M. Ruzzene, Edge waves in plates with resonators: An elastic analogue of the quantum valley Hall effect, New J. Phys. **19**, 025001 (2017).

[30] Q. Zhang, Y. Chen, K. Zhang, and G. Hu, Dirac degeneracy and elastic topological valley modes induced by local resonant states, Phys. Rev. B **101**, 014101 (2020)

[31] M. Miniaci, P. K. Pal, B. Morvan, and M. Ruzzene, Experimental Observation of Topologically Protected Helical Edge Modes in Patterned Elastic Plates, Phys. Rev. X **8**, 031074 (2018).

[32] C. W. Chen, R. Chaunsali, J. Christensen, G. Theocharis, and J. Yang, Corner states in a second-order mechanical topological insulator, Commun. Mater. **2**, 62 (2021).

[33] Z. H. Wen, S. X. Zeng, D. W. Wang, Y. B. Jin, and R. B. Djafari, Robust edge states of subwavelength chiral phononic plates, Extreme Mech. Lett. **44**, 101209 (2021).

[34] N. Gao, S. Qu, L. Si, J. Wang, W. Chen; Broadband topological valley transport of elastic wave in reconfigurable phononic crystal plate. Appl. Phys. Lett. **118** (6): 063502 (2020)

[35] H. Fan, B. Xia, L. Tong, S. Zheng, D. Yu, Elastic higher-order topological insulator with topologically protected corner states, Phys. Rev. Lett. **122**, 204301 (2019)

[36] W. Zhou, Y. Su, W.C. Muhammad, C.W. Lim. Voltage-controlled quantum valley Hall effect in dielectric membrane-type acoustic metamaterials. Int. J. Mech. Sci. **172**, 105368 (2020)

[37] Y. Chen, D. Liu, Y. Wu, P. Yu, Y. Liu, Valley Hall elastic topological insulator with large Chern numbers, Int. J. Mech. Sci. **239**, 107884 (2023)

[38] Y. Wu, M. Yan, Z. K. Lin, H. X. Wang, F. Li, and J. H. Jiang, On-chip higher-order topological micromechanical metamaterials, Sci. Bull. **66**, 1959 (2021).

[39] J. Zhao, Q. Wang, X. Wang, W. Yuan, Y. Huang, S. Chen, A. Riaud, J. Zhou, On-chip valley

phononic crystal plates with graded topological interface, Int. J. Mech. Sci. **227**,107460 (2022)

[40] Z. Chen, W. Zhou, Temperature-controlled elastic wave transport in topological ferroelectric phononic crystal plates, Int. J. Mech. Sci. **241** 107964 (2023)

[41] A. Ni, and Z. Shi, Topological metamaterial plates: Numerical investigation, experimental validation and applications. Engineering Structures **275**: 115288 (2023).

[42] S. Y. Huo, J. J. Chen, H. B. Huang, and G. L. Huang, Simultaneous multi-band valley-protected topological edge states of shear vertical wave in two-dimensional phononic crystals with veins, Sci. Rep. **7**, 10335 (2017).

[43] G.-G. Xu, X.-W. Sun, X.-D. Wen, X.-X. Liu, T. Song, and Z.-J. Liu, Valley transport via dual-band elastic topological edge states in local-resonant phononic crystal plate, J. Appl. Phys. **133**, 095110 (2023)

[44] H. Liu. Multiband topologically protected states realized by elastic honeycomb structures based on fundamental mechanical elements, Eur. J. Mech. A/Solids, **97**, 104803 (2023)

[45] W. Yuan, J. Zhao, Y. Long, J. Ren, and Z. Zhong, Multi-branch valley-chiral edge states of antisymmetric plate wave in phononic crystal plates with double-sided symmetric pillars. Int. J. Mech. Sci. **197**, 106347 (2021)

[46] Y. Chen, Z. Lan, Z. Su, and J. Zhu, Inverse design of photonic and phononic topological insulators: A review, Nanophotonics **11**, 4347 (2022).

[47] H. W. Dong, S. D. Zhao, R. Zhu, Y. S. Wang, L. Cheng, and C. Zhang. Customizing acoustic dirac cones and topological insulators in square lattices by topology optimization. J. Sound Vib **493**, 115687 (2021)

[48] Y. Chen, Z. Lan, and J. Zhu, Inversely Designed Second-Order Photonic Topological Insulator with Multiband Corner States, Phys. Rev. Appl. **17**, 054003 (2022).

[49] Y. Chen, J. Zhu, and Z. Su. Topology optimization of a second-order phononic topological

858 insulator with dual-band corner states. J. Sound Vib **544** (2023): 117410.
859 [50] Y. Chen, X. Wen, Z. Gu, J. Zhu, and Z. Su, Customizable multiband second-order sonic
860 topological insulators via inverse design, Int. J. Mech. Sci. **260** 108669 (2023)
861 [51] Z. Du, J. Luo, Z. Xu, Z. Jiang, X. Ding, T. Cui, and X. Guo, Higher-order topological insulators
862 by ML-enhanced topology optimization, Int. J. Mech. Sci. **255** 108441 (2023)
863 [52] L. Yang, K. Yu, Y. Wu, R. Zhao and S. Liu, Topological spin-Hall edge states of flexural wave in
864 perforated metamaterial plates, J. Phys. D: Appl. Phys. **51** 325302 (2018)
865 [53] S. Y. Yu, C. He, Z. Wang, F. K. Liu, X. C. Sun, Z. Li, H. Z. Lu, M. H. Lu, and Y. F. Chen, Elastic
866 pseudospin transport for integratable topological phononic circuits, Nat. Commun. **9**, 3072 (2018).
867 [54] S. An, T. Liu, H. Fan, H. Gao, Z. Gu, S. Liang, S. Huang, Y. Zheng, Y. Chen, L. Cheng, and J.
868 Zhu, Second-order elastic topological insulator with valley-selective corner states, Int. J. Mech. Sci.
869 **15**, 107337 (2022).
870 [55] Z.-D. Zhang, S.-Y. Yu, M.-H. Lu, and Y.-F. Chen. Dual-Band Helical Edge States and Discrete
871 Dirac Vortices in Solid-State Elastic Waves, Phys. Rev. Applied **17**, 034029 (2022)
872 [56] J. Jiao, T. Chen, and D. Yu. Observation of topological valley waveguide transport of elastic waves
873 in snowflake plates. Composite Structures **286**: 115297 (2022)
874 [57] B. Ungureanu, M. P. Makwana, R. V. Craster, and S. Guenneau, Localizing Elastic Edge Waves
875 via the Topological Rainbow Effect, Phys. Rev. Applied **15**, 014057, (2021)
876 [58] F. Hong, K. Zhang, L. Qi, B. Ding, Z. Deng, High-frequency topological corner and edge states
877 in elastic honeycomb plates, Int. J. Mech. Sci. **246** 108141 (2023)
878 [59] L. Fan, Y. Chen, S. An, T. Liu, H. Fan, J. Zhu, and Z. Su, Local-Resonance-Induced Dual-Band
879 Topological Corner States of Flexural Waves in a Perforated Metaplate, Phys. Rev. Applied **19**, 034065,
880 (2023)
881 [60] R.D. Mindlin. Thickness-shear and flexural vibrations of crystal plates. J. Appl. Phys. **22** (3), 316-

882 323 (1951)
883 [61] Jr, E. J. P. Miranda, E. D. Nobrega, S. F. Rodrigues, Jr, C. Aranas, and J. M. C. Dos Santos, Wave
884 attenuation in elastic metamaterial thick plates: Analytical, numerical and experimental investigations.
885 Int. J. Solids Struct **204**, 138-152 (2020)
886 [62] D. Beli, J.R.F. Arruda, M. Ruzzene, Wave propagation in elastic metamaterial beams and plates
887 with interconnected resonators, Int. J. Solids Struct, **139** 105-120 (2018)
888 [63] J. Gazalet, S. Dupont, J. C. Kastelik, Q. Rolland, and B. D. Rouhani, A tutorial survey on waves
889 propagating in periodic media: Electronic, photonic and phononic crystals. Perception of the Bloch
890 theorem in both real and Fourier domains. Wave Motion, **50**(3), 619-654 (2013)
891 [64] W. Zhu, Y. Long, H. Chen, and J. Ren, Quantum valley Hall effects and spin-valley locking in
892 topological Kane-Mele circuit networks, Phys. Rev. B **99**, 115410 (2019).
893 [65] Z. L. Du, H. Chen, and G. L. Huang, Optimal quantum valley Hall insulators by rationally
894 engineering Berry curvature and band structure, J. Mech. Phys. Solids **135**,
895 103784 (2020).
896 [66] J. Liu, Z. Ma, J. Gao, and X. Dai, Quantum Valley Hall Effect, Orbital Magnetism, and Anomalous
897 Hall Effect in Twisted Multilayer Graphene Systems, Phys. Rev. X **9**, 031021 (2019).
898 [67] Y. Eisenberg, Y. Barlas, E. Prodan, Valley Chern effect with LC resonators: a modular platform,
899 Phys. Rev. Appl., **11** (4) (2019), p. 44077
900 [68] J. Lu, C. Qiu, M. Ke, and Z. Liu, Valley Vortex States in Sonic Crystals. Phys. Rev. Lett. **116**,
901 093901 (2016)
902 [69] X. Han, Y.-G. Peng, L. Li, Y. Hu, C. Mei, D.-G. Zhao, X.-F. Zhu, and X. Wang, Experimental
903 Demonstration of Acoustic Valley Hall Topological Insulators with the Robust Selection of C3v-
904 Symmetric Scatterers, Phys. Rev. Appl.**12**, 014046 (2019).
905 [70] D. Xiao, M.C. Chang, Q. Niu, Berry phase effects on electronic properties. Rev. Mod. Phys., **82**

(3) (2010), p. 1959

[71] Y. Liu, X. Chen, and Y. Xu, Topological phononics: From fundamental models to real materials, Adv. Funct. Mater. **30**, 1904784 (2020).

[72] H. Zhu, T.-W. Liu, and F. Semperlotti, Design and experimental observation of valley-Hall edge states in diatomic-graphene-like elastic waveguides, Phys. Rev. B **97**, 174301 (2018).

[73] J. M. D. Ponti, L. Iorio, G. J. Chaplain, A. Corigliano, R. V. Craster, and R. Ardito, Tailored Topological Edge Waves via Chiral Hierarchical Metamaterials. Phys. Rev. Applied **19**, 034079 (2023)

[74] M. Wang, W. Zhou, L. Bi, C. Qiu, M. Ke, Z. Liu, Valley-locked waveguide transport in acoustic heterostructures, Nat Commun, **11** 3000 (2020)

[75] K. Chen, X. Dong, P. Gao, J. Zhang, Y. Sun, G. Tu, Z. Peng, Multifunctional applications of topological valley-locked elastic waves. Int. J. Mech. Sci. **259**, 108589 (2023)

[76] X. Zhang, L. Liu, M.-H. Lu, and Y.-F. Chen, Valley-Selective Topological Corner States in Sonic Crystals. Phys. Rev. Lett. **126**, 156401 (2021)

[77] Y. Xu, Y. Shen, F. Liu, L. Cao, Z. Yang, Modulated flexural edge waves in a plate with its free edge structured by an array of grooves. J. Sound Vib., **536** 117173 (2022)

[78] Y. Shen, Y. Xu, F. Liu, Z. Yang, Metasurface-guided flexural waves and their manipulations. Int. J. Mech. Sci. **257** 108538 (2023)

[79] M. Jung, Y. Yu, and G. Shvets, Exact higher-order bulk-boundary correspondence of corner-localized states, Phys. Rev. B **104**, 195437 (2021).

[80] H. X. Wang, G. Y. Guo, J. H. Jiang, Band topology in classical waves: Wilson-loop approach to topological numbers and fragile topology. New. J. Phys **21**(9):093029 (2019)

[81] H. Xue, Y. Yang, F. Gao, Y. Chong, B. Zhang, Acoustic higher-order topological insulator on a kagome lattice. Nat Mater, **18** 108-112 (2019)